Moiré Exciton Landscape and its Optical Properties in Two-Dimensional Semiconductors

Joakim Hagel

Department of Physics

CHALMERS UNIVERSITY OF TECHNOLOGY

Göteborg, Sweden 2022

Moiré Exciton Landscape and its Optical Properties in Two-Dimensional Semi-conductors
Joakim Hagel

Department of Physics
Chalmers University of Technology
SE-412 96 Göteborg
Sweden
Telephone + 46 (0)31-772 1000

Cover illustration: Schematic illustration of a zone-folded Brillouin and parabolic dispersion that couple via tunneling to form a hybrid exciton.

Moiré Exciton Landscape and its Optical Properties in Two-Dimensional Semiconductors
Joakim Hagel
Department of Physics
Chalmers University of Technology

Abstract

In recent years the emergence of atomically thin nanomaterials has led to a new research venue, revealing intriguing properties making them an excellent platform to study many-particle quantum phenomena. Of particular interest is the class of nanomaterials called transition metal dichalcogenides (TMDs), where the strong light-matter coupling reveals promising opportunities in the pursuit of novel optoelectronical devices. Additionally, the two-dimensional nature of TMDs leads to a strong Coulomb interaction, resulting in the formation of excitons, which are tightly bound electron-hole pairs. Due to their large binding energy, they are stable at room temperature and dominate the optical response of these materials. Furthermore, TMD monolayers can be stacked on top of each other to form heterostructures. Introducing a twist angle gives rise to a moiré pattern, allowing for the formation and trapping of highly tunable moiré excitons.

The aim of this thesis is to investigate, on a microscopic footing, the moiré exciton landscape and the many-particle mechanisms governing the optical response of TMD heterostructures. In particular, the focus lies on the impact of the moiré potential on the optical response and how the moiré exciton landscape can be externally tuned. For this purpose, we will shed light on the importance of interlayer hybridization in both twisted and untwisted TMD bilayers. We show how the hybridization can be tuned by applying an external electrical field and can turn materials into indirect semiconductors with dark excitons becoming the lowest states. Overall, the work provides microscopic insights into the twist-angle dependent optical fingerprint of the technologically promising class of atomically thin nanomaterials.
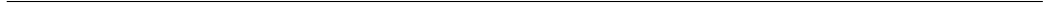
List of publications

This thesis contains an introductory text based on the following papers:

I. **Exciton landscape in van der Waals heterostructures**
J. Hagel, S. Brem, C. Linderälv, P. Erhart, E. Malic
Phys. Rev. Research. **3**, 043217 (2021)

II. **Electrical tuning of moiré excitons in MoSe$_2$ bilayers**
J. Hagel, S. Brem, E. Malic
Submitted 2022 (Preprint: arXiv:2207.01890)

My contributions to the appended papers
As first-author, I developed the microscopic theory, performed the numerical calculations, analyzed the results and wrote the papers with input from my main supervisor.

Publications outside the scope of this thesis

III. **The moiré potential in twisted transition metal dichalcogenide bilayers**
C. Linderälv, J. Hagel, S. Brem, E. Malic, P. Erhart
Submitted 2022 (Preprint: arXiv:2205.15616)

IV. **Probing P- and CP-violation in dark matter interactions**
R. Catena, J. Hagel, C. E. Yaguna
JCAP. **05**, 016 (2021)

My contributions to the non-appended publications
In paper III. I developed the theory and performed the numerical calculations for the exciton analysis in the paper. In addition, I also contributited with the discussion concerning excitons in the manuscript. In paper IV. I performed the numerical analysis as part of a master thesis project and I provided the figures for the manuscript.

Acknowledgements

First and foremost I would like to extend my gratitude to my supervisor Ermin Malic for his constant support and inspiration. The importance of your guidance in my development as a researcher cannot be understated. Secondly, I want to thank my colleague Samuel Brem for his essential part in the projects that have laid the foundation for this thesis. Your intuition into the field of exciton physics is truly inspiring and I look forward to many more future discussions. I would also like to extend my thanks to my examiner Jari Kinaret for reading my thesis and providing valuable feedback, thus increasing the quality of this work.

Furthermore, I would like to thank all my colleagues in the Ultrafast Quantum Mechanics group, with a special thank you going out to Raul Perea Causin and Daniel Erkensten for their constant willingness to engage in discussion. The lunch breaks are rarely boring with you two around.

Finally, I want to thank my friends and family for supporting me during this endeavor, and even more importantly, keeping me grounded. Tack!

CONTENTS

CHAPTER 1

INTRODUCTION

In 2004, the atomically thin nanomaterial graphene was successfully isolated for the first time [1], a discovery later rewarded with the Nobel Prize for physics [2]. The intriguing properties displayed by graphene [3] later paved the way for a whole new class of nanomaterials called two-dimensional materials [4]. Due to the crystal dimensionality, the motion of the electron is restricted to two dimensions in these materials, in turn leading to fascinating new physics and promising concepts of novel technological devices. One of the most promising materials from this new class are the transition metal dichalcogenides (TMDs) [5, 6] (cf. Fig 1.1).

TMDs are particular interesting due to their optical properties [7]. Here, the two-dimensional nature give rise to a reduced screening of the Coulomb potential. Consequently, an electron in the conduction band can become strongly bound with the electron vacancy in the valance band, most often refereed to as holes [6]. This bound state is known as an exciton and fundamentally changes the optical response of the material [8]. Other bound states involving more particles in these materials are possible, for example trions [9, 10]. This is however outside the scope of this thesis. Furthermore, by stacking two sheets of TMDs on top of each other to form van der Waals heterostructures [11], long lived interlayer excitons can form [12–18]. Here, the electron and hole is spatially separated by belonging to different layers.
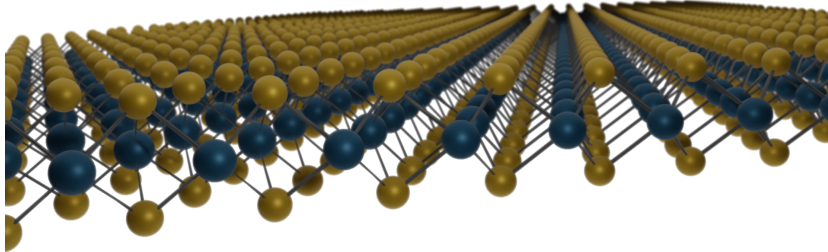
Figure 1.1: Illustration of a monolayer TMD.

This in turn gives this new exciton species some intriguing properties in comparison to the excitons that are confined to one layer. Importantly for this work, they exhibit an out-of-plane dipole moment which allows for external tuning of the energies via electrical fields [19, 20]. The introduction of vertically stacked TMDs also allows for overlapping electronic wavefunctions between the layers, which leads to interlayer tunneling of carriers. Consequently, hybrid excitons hX can form that have both an interlayer exciton IX component and an intralayer exciton component X_0 (cf. Fig 1.2).

Moreover, by twisting two vertically stacked 2D materials with a honeycomb lattice one can introduce a moiré pattern (cf. Fig 1.3). It has been shown that the introduction of such a moiré patterns to vertically stacked bilayer graphene sheets lead to exotic new quantum phenomena such as Mott insulating phases and unconventional superconductivity [21], in turn clearly demonstrating exciting new opportunities to study intriguing physics in 2D materials. The same type of moiré pattern can by applied to vertically stacked TMDs, allowing for another way to tune the exciton physics via the periodic moiré potential that emerges in this new superlattice [22–26]. Also here a rich landscape of interesting physics has been revealed [27], allowing for flat exciton bands that trap excitons in real space, which heavily impacts both the exciton energy landscape and the optical response [28, 29].

In this work we investigate the exciton energy landscape and its optical re-
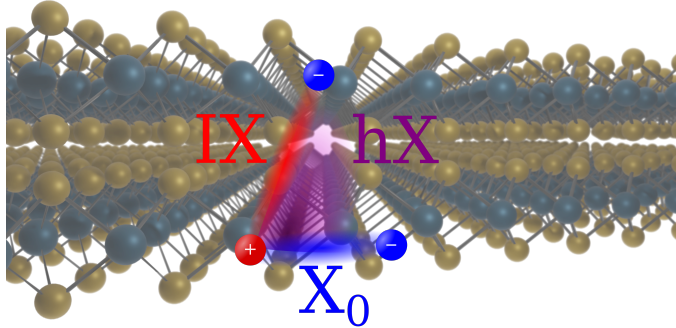
Figure 1.2: Illustration of bilayer TMD with a hybrid exciton hX made out of an interlayer component IX and an intralayer component X_0.

sponse in bilayer TMD structures. The focus lies on the interplay between different components of the moiré potential. Furthermore, we exploit the gained insights in order to externally tune the exciton energy landscape via twist angle engineering or applied electrical fields. We find that the interlayer hybridization plays a major role for of the exciton energy landscape, making momentum dark excitons dominate in many bilayer TMDs (paper I.). Additionally, we calculate the optical response for twisted bilayer $MoSe_2$ under the influence of an external electric field, revealing interlayer hybridization as the cause for distinct regions in the photoluminescence spectra (paper II.), dominated by either intralayer or interlayer excitons, or even dark excitons. Consequently, we predict critical field strengths as a function of twist angle where one can turn the material from a direct to an indirect semiconductor. Overall, our work provides novel microscopic insights into the quantum many-body processes that govern the moiré exciton physics in this intriguing class of nanomaterials.

The thesis has been organized in the following way. We start by introducing the theoretical framework (chapter 2) used throughout this work, beginning with a brief introduction into second quantization and density matrix formalism, then continuing with the Hamiltonian representation of many-particle processes that we are interested in and how excitons can be treated within this formalism. Chapter 3 summarizes the work done in paper I. and details how the different components of the moiré potential affect the exciton energy landscape in untwisted structures. Here, we discuss our developed
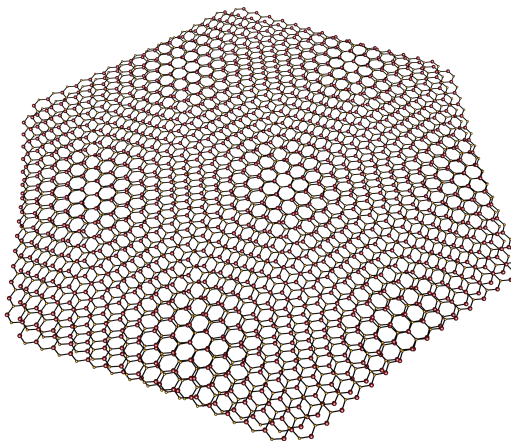
Figure 1.3: Illustration of moiré pattern with twisted TMDs.

model for the interlayer hybridization and how it affects the optical response of the material. We then investigate how the previous insights can be exploited for external tuning of the optical response of moiré excitons (paper II.). Moreover, we generalize the framework to include twisted structures and also applied electrical fields. We end with some concluding remarks and outlook.

CHAPTER 2

THEORETICAL FRAMEWORK

In this chapter we present the underlying theory used throughout the thesis and in the appended works. Starting with a brief introduction to the density matrix formalism and second quantization, then continuing with the many-particle Hamiltonian in TMDs. Finally, we discuss the concept of excitons and how the Hamiltonian can be simplified by considering a transformation into exciton basis.

2.1 Second quantization and density matrix formalism

Second quantization

In this work we make use of second quantization in order to model the fundamental statistical properties of the particles found in these condensed matter systems. Since the topic of second quantization can be found in most condensed matter physics textbooks, we will only briefly cover the essentials here.

In the many-particle systems we are interested in, we have a vast unknown

number of identical quantum particles. This would in quantum mechanics be described by an N-particle wavefunction Ψ_N [30]. The construction and computation of this N-particle wavefunction is often too tedious or difficult to be practically feasible. In second quantization we instead capture the fundamental statistical properties with the introduction of creation $a^\dagger$ and annihilation operators a. Here, we can describe a many-particle state $|\phi_1\phi_2...\phi_N\rangle$ with the use of these operators acting upon a single state $a_1^\dagger a_2^\dagger...a_N^\dagger |0\rangle$ [30]. We can then interpret $a_i^\dagger$ as creating an additional particle in the single state $|\phi_i\rangle$. Since the annihilation operator a_i is the Hermitian adjoint of $a_i^\dagger$, this can reversely be thought of as annihilating a particle in the single state $|\phi_i\rangle$.

The fundamental statistical properties of particles, stemming from the spin statistics theorem, is captured by two distinct particle descriptions. Either the particle has integer spin - boson - or it has half-integer spin - fermion -, where fermions obey the Pauli exclusion principle and bosons do not, i.e two fermions can not occupy the same state. In our current framework this translates into whether the many-particle state $|\phi_1\phi_2...\phi_N\rangle$ is symmetric or anti-symmetric under Permutation (or exchange) $\widehat{\mathcal{P}}$ [30] [1]. The many-particle state is symmetric for bosons

$$\widehat{\mathcal{P}}_{12} |\phi_1\phi_2...\phi_N\rangle = |\phi_2\phi_1...\phi_N\rangle , \qquad (2.1)$$

and anti-symmetric for fermions

$$\widehat{\mathcal{P}}_{12} |\phi_1\phi_2...\phi_N\rangle = - |\phi_2\phi_1...\phi_N\rangle . \qquad (2.2)$$

From this principle we can easily read of the essential commutators we need for a and $a^\dagger$, thus finding that bosons commute

$$[a_i^{(\dagger)},a_j^{(\dagger)}] = a_i^{(\dagger)}a_j^{(\dagger)} - a_j^{(\dagger)}a_i^{(\dagger)} = 0, \quad [a_i,a_j^\dagger] = \delta_{ij}, \qquad (2.3)$$

and fermions anti-commute

$$\{a_i^{(\dagger)},a_j^{(\dagger)}\} = a_i^{(\dagger)}a_j^{(\dagger)} + a_j^{(\dagger)}a_i^{(\dagger)} = 0, \quad \{a_i,a_j^\dagger\} = \delta_{ij}. \qquad (2.4)$$

With these simple commutation rules, the fundamental statistical properties of the many-particle state is captured, allowing us to efficiently model the different particles determining the physics in our nanomaterials.

---

[1]In two dimensions there are exceptions to this rule where a particle called anyon instead has a phase and is not as restricted as the conventional fermion and boson [31, 32].

Density matrix formalism
In combination with second quantization we use the density matrix formalism. Here, the density matrix ρ is a statistical ensemble of of many quantum states [30],

$$\rho = \sum_n p_n \left| \Psi_n \right\rangle \left\langle \Psi_n \right|, \tag{2.5}$$

where p_n is the corresponding probability to find a particle in state $\left| \Psi_n \right\rangle$. Within this formalism we can associate the expectation value of a quantum mechanical observable $\langle \mathcal{O} \rangle$ to the trace of the density matrix [30],

$$\langle \mathcal{O} \rangle = \sum_n p_n \left\langle \Psi_n | \mathcal{O} | \Psi_n \right\rangle = tr(\rho \mathcal{O}), \tag{2.6}$$

where $tr(\rho^2) = 1$ for pure states and $tr(\rho^2) < 1$ for mixed states. Using this definition of expectation values we can separate the temporal evolution of $\langle \mathcal{O} \rangle$ into two parts, one coherent part $\langle \mathcal{O} \rangle_{coh}$ and one scattering $\langle \mathcal{O} \rangle_{sca}$ part [33]. Importantly for this work, we can then recognize the coherent part as the particle occupation probability $\langle a_i^\dagger a_i \rangle$ and the scattering part as the microscopic polarization $\langle a_i^\dagger a_j \rangle$.

2.2 Many-particle Hamiltonian in TMDs

Now when the fundamental theoretical principles has been established we can set up a Hamiltonian for our interacting particles in the TMDs. For the processes covered in this work we mainly focus on three particles and their corresponding interactions; electrons, photons and phonons. Before looking closer at the various interactions that occurs, we will first establish the free kinetic part of the Hamiltonian.

Free Hamiltonian
The free Hamiltonian describing the kinetic energy for electrons or holes is simply given by

$$H_{el,0} = \sum_{\boldsymbol{k}\lambda} \varepsilon_{\boldsymbol{k}}^\lambda \lambda_{\boldsymbol{k}}^\dagger \lambda_{\boldsymbol{k}}, \tag{2.7}$$

where $\lambda = (c,v)$ is describing either electrons in the conduction band c or holes in the valance band v. Here $\boldsymbol{k}$ is the momentum in the Brillouin zone
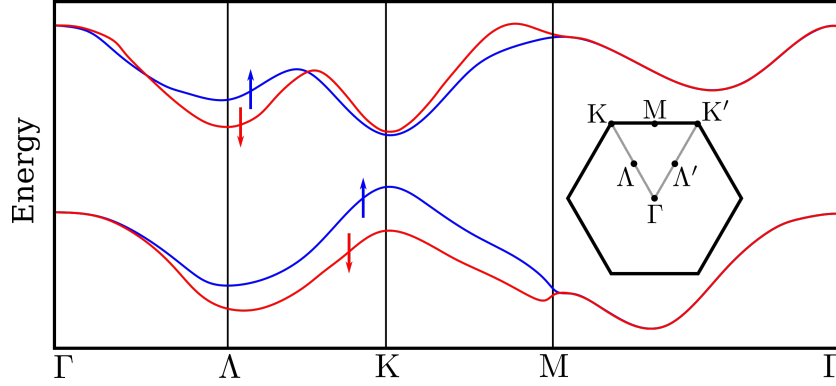
Figure 2.1: Schematic for a typical TMD bandstructure. The local minima for the conduction band and maxima for the valance band can be found along the high symmetry points. Arrows indicate the difference in spin configuration. The figure is adapted from Ref. [35].

and $\varepsilon_{\boldsymbol{k}}^{\lambda}$ is the associated kinetic energy. A schematic for a typical TMD bandstructure can bee seen in Fig 2.1. Here, the local conduction band minima and valance band maxima can be found around the high symmetry points in the Brillouin zone (BZ) [2], which in general are the points of interest when considering excitons. Furthermore, the dispersion around these high symmetry points is well approximated by a parabolic dispersion. Thus, the electrons and holes can be considered as free particles with an effective mass.

The second part of the free Hamiltonian is given by the free phonon part

$$H_{ph,0} = \sum_{\boldsymbol{k}_{ph}j} \hbar\Omega_{\boldsymbol{k}_{ph}}^{j} b_{\boldsymbol{k}_{ph}j}^{\dagger} b_{\boldsymbol{k}_{ph}j}, \tag{2.8}$$

where $\boldsymbol{k}_{ph}$ is the phonon momentum and $j = $ (TA,LA,LO,TO,A1) is the phonon mode index, which takes into account both the transverse (T) and longitudinal (L) part, in addition the the optical (O) branch and the acoustic (A) branch. Here, A1 is an out-of-plane optical mode. The phonon dispersion is given by $\Omega_{\boldsymbol{k}_{ph}j}$, where a schematic of a typical TMD phonon bandstructure can be seen in Fig 2.2. From this figure we can see that most modes have an

---

[2]The Λ point is strictly speaking not a symmetry point, but rather the midpoint in a symmetry line [34]. This distinction is however not important for the purpose of this work.
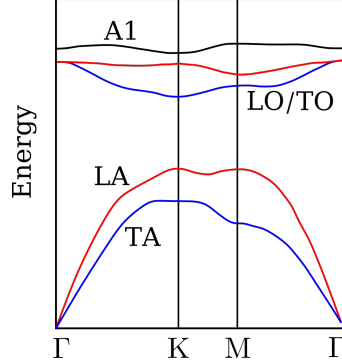
Figure 2.2: Schematic of a typical phonon bandstructure in TMDs with the relevant modes illustrated. A linear approximation is made for the acoustical modes close to the Γ point. In the vicinity of the remaining high symmetry points a constant approximation is made. Schematic adapted from Ref. [36].

approximate flat dispersion around each high symmetry point, the exception being the long range acoustical modes (close to the Γ point) which can be approximated as linear. Thus we make use of the Debye approximation for long range acoustics phonons and the Einstein approximation (flat dispersion, i.e constant) for the rest.

The remaining part of the free Hamiltonian is the photon dispersion which is simply given by

$$H_{l,0} = \sum_{\boldsymbol{k}\sigma} \hbar\omega_{\boldsymbol{k}}^{\sigma} \tilde{c}_{\boldsymbol{k}\sigma}^{\dagger} \tilde{c}_{\boldsymbol{k}\sigma}, \qquad (2.9)$$

where σ is the polarization and $\hbar\omega_{\boldsymbol{k}}^{\sigma}$ is the photon energy.

Electron-electron Hamiltonian
The formation of excitons stems from the strong Coulomb interaction between electrons and holes, which in turn makes them a tightly bound electron-hole pair. The Hamiltonian governing this interaction, often referred to as the electron-electron Hamiltonian or simply the Coulomb interaction, is given by [37]

$$H_{el-el} = \frac{1}{2} \sum_{\substack{\boldsymbol{k}\boldsymbol{k}'\boldsymbol{q} \\ \lambda\lambda'}} V_{\boldsymbol{q}} \lambda_{\boldsymbol{k}+\boldsymbol{q}}^{\dagger} \lambda_{\boldsymbol{k}'-\boldsymbol{q}}^{\prime\dagger} \lambda_{\boldsymbol{k}'}^{\prime} \lambda_{\boldsymbol{k}}, \qquad (2.10)$$

where we now have restricted the Hamiltonian to only include intraband processes with small momentum transfers. Here, $\boldsymbol{q}$ is the transferred momentum

and $V_{\boldsymbol{q}}$ is the Coulomb matrix element. When considering monolayers, the matrix element is derived from a modified form of the Rytova-Keldysh potential [38, 39], which can be obtained by solving the Poisson equation for charges in a thin film with thickness d encased in a dielectric environment. The obtained Coulomb potential then has the following expression [40]

$$V_{\boldsymbol{q}} = \frac{e^2}{2\epsilon_0 A \boldsymbol{q} \epsilon_{scr}(\boldsymbol{q})},$$ (2.11)

where A is the lattice area, e is the charge and ϵ_0 is the vacuum permittivity. The dielectric screening $\epsilon_{scr}(\boldsymbol{q})$ is given by

$$\epsilon_{scr}(\boldsymbol{q}) = \kappa_{\text{TMD}} \tanh\left(\frac{1}{2}[\alpha_{\text{TMD}} dq - \ln\left(\frac{\kappa_{\text{TMD}} - \kappa_{\text{sub}}}{\kappa_{\text{TMD}} + \kappa_{\text{sub}}}\right)]\right),$$ (2.12)

where $\kappa = \sqrt{\epsilon^{\parallel}\epsilon^{\perp}}$ and $\alpha = \sqrt{\frac{\epsilon^{\parallel}}{\epsilon^{\perp}}}$. Here, $\epsilon^{\parallel}$ accounts for the in-plane component of the dielectric tensor and $\epsilon^{\perp}$ accounts for the out-of-plane component.

Electron-phonon Hamiltonian

An important process when describing the dynamics of excitons is their interaction with phonons. For this purpose it is important to model the electron-phonon interaction, where an electron or hole can scatter with a phonon with some momentum transfer

$$H_{el-ph} = \sum_{\substack{\boldsymbol{kq} \\ j\lambda}} G_{j\boldsymbol{q}}^{\lambda} \lambda_{\boldsymbol{k+q}}^{\dagger} \lambda_{\boldsymbol{k}} (b_{j,-\boldsymbol{q}}^{\dagger} + b_{j,\boldsymbol{q}}),$$ (2.13)

where $G_{j\boldsymbol{q}}^{\lambda}$ is the electron-phonon matrix element given by [36, 37, 41],

$$G_{j\boldsymbol{q}}^{\lambda} = g_{j\boldsymbol{q}}^{\lambda} \sqrt{\frac{\hbar^2}{2\rho \mathcal{A} \hbar \Omega_{j\boldsymbol{q}}}}.$$ (2.14)

Here, ρ is the mass density and $\mathcal{A}$ is the associated density of said area. $\Omega_{j\boldsymbol{q}}$ indicate the phonon energies, which can be extrapolated from a bandstructure like Fig 2.2. The electron-phonon coupling is given by $g_{j\boldsymbol{q}}^{\lambda}$, which in a similar fashion as the energy is approximated as constant for all modes except for the long range acoustical modes that are approximated as linear in $\boldsymbol{q}$. The material and valley specific value of these couplings are obtained from first-principle calculations done in [36, 41].

Electron-light Hamiltonian

In this work we treat the electron-light interaction in two different approaches, depending on the process we wish to model [3]. In the case for optical excitation of an electron, we treat the electron-light interaction in the semi-classical way, i.e an electron interacting with an electromagnetic field. As long as we only consider this optical absorption in the material, this is a sufficient approach. Here the electron-light Hamiltonian reads

$$H_{el-l} = -i\hbar \frac{e_0}{m_0} \sum_{\boldsymbol{k}\lambda\lambda'} \boldsymbol{M}_{\boldsymbol{k}}^{\lambda\lambda'} \cdot \boldsymbol{A}(t) \lambda_{\boldsymbol{k}}'^{\dagger} \lambda_{\boldsymbol{k}}, \qquad (2.15)$$

where $\boldsymbol{M}_{\boldsymbol{k}}^{\lambda\lambda'} = \langle \lambda'\boldsymbol{k} | \nabla | \lambda\boldsymbol{k} \rangle$ is the optical matrix element, $\boldsymbol{A}(t)$ is the electromagnetic vector potential. Here e_0 and m_0 is the elementary charge and free electron mass respectively. Within the scope of this work, we are mainly interested in the interband transitions, that is $\lambda' = c$ and $\lambda = v$. This then describes the optical excitation of an electron which consequently can form an exciton.

If we instead want to consider the emission of light from the material this semi-classical description is not sufficient. Here we instead have the emission of a photon after an electron has been optically excited. Since we are here dealing with the electron interacting with a single photon a more complete quantum mechanical framework is needed. For this purpose we have the electron-photon Hamiltonian which reads

$$H_{el-photon} = \sum_{\sigma \boldsymbol{q} \boldsymbol{k} \lambda\lambda'} \boldsymbol{M}_{\boldsymbol{k}\sigma}^{\lambda\lambda'} \lambda_{\boldsymbol{k}+\boldsymbol{q}\|}^{\dagger} \lambda_{\boldsymbol{k}}' \tilde{c}_{\boldsymbol{q}}^{\dagger} + h.c, \qquad (2.16)$$

where $\boldsymbol{M}_{\boldsymbol{k}\sigma}^{\lambda\lambda'}$ again is the optical matrix element and $\boldsymbol{q} \parallel$ is the momentum that is parallel to the monolayer. In this work we mainly focus on the relaxation of an electron from the conduction band to the valance band, i.e $v^{\dagger}c\tilde{c}$. This is then the Hamiltonian of interest when considering a photoluminescence spectrum.

---

[3]By placing the material in a cavity, the light-matter interaction can also lead to the formation of exciton-polaritons [42, 43]. This is however outside the scope of this thesis.

2.2.1 Equation of motion

By having complete access to the Hamiltonian that describe the system we can calculate the temporal evolution of some observable $\mathcal{O}$. This is done via Heisenbergs equation of motion [37][4].

$$i\hbar\frac{d}{dt}\left\langle\mathcal{O}\right\rangle = \left\langle[\mathcal{O},H]_-\right\rangle. \tag{2.17}$$

As mention in 2.1 we can via the density matrix approach separate the particle occupation from the microscopic polarization and thus calculate the temporal evolution of these separately. This means when considering excitons it is sufficient to commute the polarization $\langle c^\dagger v\rangle$ with the Hamiltonian [5]

2.2.2 Cluster expansion approach

An often occurring problem in many-particle physics is higher order correlations and how to truncate them. If we for example want to calculate the temporal evolution for the microscopic polarization $\langle a_1^\dagger a_2\rangle$ we will find that it couples to a two particle correlation $\langle a_i^\dagger a_j^\dagger a_k a_l\rangle$. This quantity does in turn couple to a three particle quantity which in turn couples to higher order correlations, leading to a system of differential equations which are not closed, a problem often refereed to as the hierarchy problem. In order to solve this equation a scheme to factorize and truncate away the higher order correlations is needed. This can be done by expressing the N-particle quantity as single particle quantities, also known as singlet, and a higher order correction. A common cluster expansion and truncation scheme is the well known Hartree-Fock approximation [37]

$$\langle a_i^\dagger a_j^\dagger a_k a_l\rangle = \langle a_i^\dagger a_l\rangle\langle a_j^\dagger a_k\rangle - \langle a_i^\dagger a_k\rangle\langle a_j^\dagger a_l\rangle + \langle a_i^\dagger a_j^\dagger a_k a_l\rangle_{\text{cor}}, \tag{2.18}$$

---

[4]This is not to be confused with the von Neuman equation. Although being similar, instead deals with the temporal evolution of the density matrix itself, not an operator.

[5]In this work we are mainly interested in the microscopic polarization, but importantly for exciton diffusion [44] one can also calculate the equation of motion of the particle occupation.

where the two particle correlation has been factorized as singlets and a higher order correction. We can then neglect this higher order correction and successfully simplify the equation of motion to a single particle problem, which can be solved.

2.2.3 Markov approximation

The optical responses studied in this work often comes in the form of phonon-assisted photoluminescence. Here, the electron-phonon interaction is very important and in these cases the inclusion of higher order correlations will often be necessary. In these problems one will encounter the two particle correlation $S = \langle a^\dagger a b^\dagger \rangle$, which yields the following form for the equation of motion

$$\dot{S}(t) = (i\omega - \gamma)S(t) + P(t). \tag{2.19}$$

In order to solve this equation we make use of the Markov approximation, where we take the standard analytical solution

$$S(t) = \int_0^\infty d\tau e^{i\omega - \gamma} P(t - \tau), \tag{2.20}$$

and neglect the past values of $P(t)$, i.e $P(t - \tau) \approx P(t)e^{-i\omega_P \tau}$. Here P is now approximated at its current time with some temporal oscillation ω_P. With this approximation the integral can now be solved

$$S(t) = \frac{P(t)}{\gamma + i(\omega - \omega_P)}, \tag{2.21}$$

and by applying the Sokhotski–Plemelj theorem for $\gamma \to 0$ we have the following expression

$$S(t) = \pi P(t)\delta(\omega - \omega_P) - i\mathcal{P}\Big(\frac{P(t)}{\omega - \omega_P}\Big). \tag{2.22}$$

Here, the first term is usually contributing to the scattering rate, which is often the point of interest. $\mathcal{P}$ is instead the principal value which often contributes to an energy renormalization, something which can be neglected in most cases.

2.3 Excitons

In the previous section we presented the relevant Hamiltonian operators for the processes considered in this work. These Hamiltonians are, however, given in electron hole-basis which can often become cumbersome and impractical to work with, especially when considering exciton dynamics. In order to reduce the number of operators we work with and thus the complexity, an additional framework is needed. In this section we go through how one can go from the electron-hole Hamiltonian to an exciton Hamiltonian and directly incorporate the Coulomb interaction into the free exciton part.

2.3.1 Wannier equation

An exciton becomes strongly bound due to the Coulomb interaction between electrons and holes. In order to calculate these binding energies we need to calculate the temporal evolution of the microscopic polarization $p_{\boldsymbol{kk'}} = \langle c_{\boldsymbol{k}}^{\dagger} v_{\boldsymbol{k'}} \rangle$, which is done via Eq. 2.17. Importantly, by commuting this operator quantity with the Coulomb interaction (Eq. 2.10) and then applying the Hartree-Fock approximation (Eq. 2.18), the resulting expression is the well known semi-conductor Bloch equation [33],

$$i\hbar \dot{p}_{\boldsymbol{kk'}} = (\varepsilon_{\boldsymbol{k}}^{v} - \varepsilon_{\boldsymbol{k'}}^{c})p_{\boldsymbol{kk'}} + \sum_{\boldsymbol{q}} V_{\boldsymbol{q}} p_{\boldsymbol{k+q,k'+q}} + \tilde{\Omega}_{\boldsymbol{kk'}}, \qquad (2.23)$$

where we have assumed a low excitation regime, i.e that the occupation lies with the valance band. The first term in the equation is simply the band edge energy of the electron/hole pair and the second term takes into account the Coulomb attraction between the electron and hole. Furthermore, the last term $\tilde{\Omega}_{\boldsymbol{kk'}} = i\hbar \frac{e_0}{m_0} \boldsymbol{M}_{\boldsymbol{k}}^{vc} \cdot \boldsymbol{A}(t)\delta_{\boldsymbol{kk'}}$ is the Rabi frequency that accounts for optical polarization.

The above equation can be simplified by writing it in terms of center-of-mass coordinates $\boldsymbol{Q} = \boldsymbol{k}_e - \boldsymbol{k}_h$, $\boldsymbol{k} = \alpha \boldsymbol{k}_h + \beta \boldsymbol{k}_e$. Here, $\alpha = m_e/(m_e + m_h)$ and $\beta = m_h/(m_e + m_h)$. The effective masses of the electrons and holes can be approximated with a parabolic approximation around each high symmetry point from a bandstructure calculated with first-principle calculations (such

as Fig 2.1) [35]. Equation 2.23 then reads

$$i\hbar \dot{p}_{\boldsymbol{Q}\boldsymbol{k}} = -\varepsilon_{\boldsymbol{Q}\boldsymbol{k}} p_{\boldsymbol{Q}\boldsymbol{k}} + \sum_{\boldsymbol{q}} V_{\boldsymbol{q}} p_{\boldsymbol{Q},\boldsymbol{k}+\boldsymbol{q}} + \tilde{\Omega}_{\boldsymbol{0}}, \tag{2.24}$$

where $\tilde{\Omega}_{\boldsymbol{0}}$ is constrained to $\boldsymbol{Q} = \boldsymbol{0}$ from the momentum selection rules and $\varepsilon_{\boldsymbol{Q}\boldsymbol{k}}$ is the kinetic energy of the electron(hole) which is given by

$$\varepsilon_{\boldsymbol{Q}\boldsymbol{k}} = E_{gap} + \frac{\hbar^2 \boldsymbol{Q}^2}{2M} + \frac{\hbar^2 \boldsymbol{k}^2}{2m_{red}}. \tag{2.25}$$

Here the center-of-mass momentum $\boldsymbol{Q}$ is shifted by some valley coordinate $\boldsymbol{\xi} = (\xi_e, \xi_h)$ and E_{gap} denotes the bandgap energy. Furthermore, $M = m_e + m_h$ is the total mass and $m_{red} = m_e m_h/(m_e + m_h)$ is the reduced mass. We now introduce the basis change $p_{\boldsymbol{Q}\boldsymbol{k}} = \sum_{\mu} P_{\boldsymbol{Q}}^{\mu} \Psi^{\mu}(\boldsymbol{k})$, where μ is exciton quantum number (For the purpose of bilayers in chapter 3 and chapter 4 this is restricted to 1s.) and $\Psi^{\mu}(\boldsymbol{k})$ is a complete set of orthogonal eigenvectors that satisfy the following eigenvalue problem

$$\frac{\hbar^2 \boldsymbol{k}^2}{2m_{red}} \Psi_{\boldsymbol{\xi}}^{\mu}(\boldsymbol{k}) - \sum_{\boldsymbol{q}} V_{\boldsymbol{q}} \Psi_{\boldsymbol{\xi}}^{\mu}(\boldsymbol{k}+\boldsymbol{q}) = E_{\boldsymbol{\xi}}^{\mu} \Psi_{\boldsymbol{\xi}}^{\mu}(\boldsymbol{k}). \tag{2.26}$$

Here, the eigenvalue problem has been written specifying the valley $\boldsymbol{\xi}$, consequently we can drop the dependence on $\boldsymbol{Q}$. This equation is then similar to the Schrödinger equation and solves for the exciton bindings energies $E_{\boldsymbol{\xi}}^{\mu}$ and exciton wavefunctions $\Psi_{\boldsymbol{\xi}}^{\mu}(\boldsymbol{k})$.

By solving Eq. 2.26, which is known as the Wannier equation, we can then gain access to the exciton binding energies for a specific valley configuration. Most commonly we think of the electron and hole sitting around the same high symmetry point in the bandstructure. i.e the center-of-mass momentum $\boldsymbol{Q} = \boldsymbol{0}$, but we can also have momentum indirect excitons, known as dark excitons (In contrast, an exciton where the electron and hole sits in the same valley is called bright.) (cf. Fig 2.3) [45–47]. Here, the electron and hole are separated by some momentum in the Brillouin zone and can thus not be optically excited. As we will see later in this work however, these excitons will become very important when describing other optical features, especially in bilayers, thus it is important to take them into consideration.
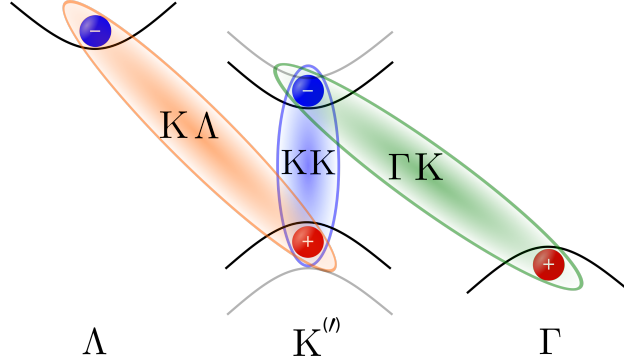
Figure 2.3: Schematic for different exciton valley configurations. Here we can see the bright KK exciton and the momentum dark KΛ/ΓK exciton. The shaded lines at the K indicate the K′ valley, which instead can form the spin-dark exciton KK′.

Applying this basis change into Eq. 2.24 we then have the semi-conductor Bloch equation in exciton basis

$$i\hbar \dot{P}^{\mu}_{\boldsymbol{Q}} = -E^{\mu}_{\boldsymbol{Q}} P^{\mu}_{\boldsymbol{Q}} - \Omega^{\mu}_{\boldsymbol{0}}, \tag{2.27}$$

where

$$E^{\mu}_{\boldsymbol{Q}} = E_{gap} + \frac{\hbar^2 \boldsymbol{Q}^2}{2M} + E^{\mu}_{\boldsymbol{\xi}}, \quad \Omega^{\mu}_{\boldsymbol{0}} = \frac{e_0}{m_0} \sum_{\boldsymbol{k}} \Psi^{\mu}_{\boldsymbol{\xi}}(\boldsymbol{k})^* \boldsymbol{M}^{vc}_{\boldsymbol{k}} \cdot \boldsymbol{A}(t). \tag{2.28}$$

The solution to this equation can then easily be found by Fourier transforming the equation into frequency space, which then reads

$$P^{\mu}_{\boldsymbol{Q}}(\omega) = \frac{\Omega^{\mu}_{\boldsymbol{0}}(\omega)}{\hbar\omega - E^{\mu}_{\boldsymbol{0}} - i\gamma}, \tag{2.29}$$

where we have introduced the phenomenological damping γ.

2.3.2   Exciton basis

In the previous section we showed that one can transform the semi-conductor Bloch equation into exciton basis and thus incorporate the Coulomb interaction by solving the Wannier equation (2.26). A similar approach is possible

to apply directly to the Hamiltonian [48], thus further simplifying future calculations. First, we apply something called the pair operator expansion

$$P^\dagger_{\boldsymbol{k}\boldsymbol{k}'} = c^\dagger_{\boldsymbol{k}} v_{\boldsymbol{k}'}. \tag{2.30}$$

The commutator of this operator then reads

$$[P_{ij}, P^\dagger_{kl}] = \delta^{jl}_{ik} - \mathcal{O}_{corr}, \tag{2.31}$$

where $\mathcal{O}_{corr} = v^\dagger_l v_j \delta_{ik} + c^\dagger_k c_i \delta_{jl}$ is a correction term that accounts for the fact that excitons are composite quasiparticles from fermions. Since this correction scales with the occupation, we can at low density approximate an exciton as a fully bosonic particle, i.e

$$[P_{ij}, P^\dagger_{kl}] \approx \delta^{jl}_{ik}. \tag{2.32}$$

This also translates into intraband transitions which would transform as

$$\begin{aligned}
c^\dagger_{i\boldsymbol{k}} c_{j\boldsymbol{k}'} &\approx \sum_{m\boldsymbol{p}} P^\dagger_{i\boldsymbol{k},m\boldsymbol{p}} P_{j\boldsymbol{k}',m\boldsymbol{p}} \\
v^\dagger_{i\boldsymbol{k}} v_{j\boldsymbol{k}'} &\approx \delta^{ij}_{\boldsymbol{k}\boldsymbol{k}'} - \sum_{m\boldsymbol{p}} P^\dagger_{m\boldsymbol{p},j\boldsymbol{k}'} P_{m\boldsymbol{p},i\boldsymbol{k}}.
\end{aligned} \tag{2.33}$$

The next step is to turn these pair operators into exciton operators. This is done in similar manner as in the previous section where we expand with the exciton wavefunctions

$$P^\dagger_{\boldsymbol{k}\boldsymbol{k}'} = \sum_\mu X^\dagger_{\mu,\boldsymbol{k}-\boldsymbol{k}'} \Psi^\mu(\alpha\boldsymbol{k}' + \beta\boldsymbol{k}), \tag{2.34}$$

where $X^\dagger$ is the exciton creation operator and $\Psi^\mu(\boldsymbol{k})$ are the exciton wavefunctions. Here, μ is compound index taking into account both valley and exciton quantum number. With this transformation we can write a diagonal form of the free electronic Hamiltonian and the Coulomb interaction

$$H_{el,0} + H_{el-el} \to H_0 = \sum_{\boldsymbol{Q}\mu} E^\mu_{\boldsymbol{Q}} X^\dagger_{\mu\boldsymbol{Q}} X_{\mu\boldsymbol{Q}}. \tag{2.35}$$

By solving the Wannier equation to obtain $E^\mu_{\boldsymbol{Q}}$ (2.26) we can then turn a problem involving the interaction between two particles into a free one particle Hamiltonian as illustrated in Fig 2.4. This transformation can then be applied to all other Hamiltonians and thus moving the entire framework to exciton basis instead.
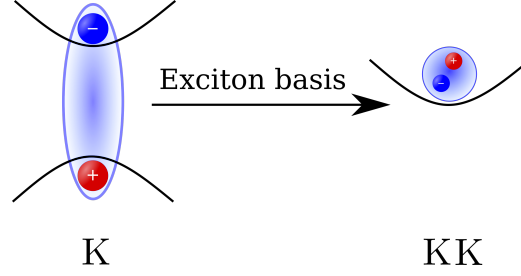
Figure 2.4: Schematic of transformation into exciton basis.

2.3.3 Elliot formula

In order to gain access to the optical response of the material we study the linear response from an electric field $\boldsymbol{E}$

$$P(\omega) = \epsilon_0 \chi(\omega) E(\omega), \tag{2.36}$$

where $P(\omega)$ is the polarization induced from the electric field and $\chi(\omega)$ is the optical susceptibility. This equation can then be rewritten

$$\chi(\omega) = \frac{j(\omega)}{\varepsilon \omega^2 A(\omega)}. \tag{2.37}$$

Here, the relationship between the electric field and the vector potential is used $E = \dot{A}(\omega)$, in combination with the relation between the polarization and the macroscopic current $j(\omega) = \dot{P}(\omega)$.

In order to connect this macroscopic response to our microscopic model we can for this purpose interpret j is the probability current, which in second quantization reads

$$j(t) = \frac{e_0 \hbar}{A m_0} \sum_{\boldsymbol{k}} \mathrm{Im}\{M_{\boldsymbol{k}} p_{\boldsymbol{kk}}\}, \tag{2.38}$$

where we now have neglected the intraband current due to its limiting impact in the sub-THZ regime. Here, we also only focus on the imaginary part since this describes the optical absorption. We can now combine the expression together with the solution to the Bloch equation in exciton basis (2.29) and plug the results into Eq. 2.37 to get the formula for optical absorption

$$\alpha(\omega) \propto \frac{1}{\omega} \sum_{\mu} \frac{|M^{\mu}|^2}{(\hbar\omega - E_{\boldsymbol{0}}^{\mu})^2 + \gamma^2}. \tag{2.39}$$

18

This equation which is known as the Elliot formula can then be used to calculate the optical response of the material taking into account the exciton features of said material [49].

CHAPTER 3

MOIRÉ EXCITON LANDSCAPE

So far we have only dealt excitons in a monolayer. In this chapter we will generalize our Hamiltonian in order to include the effects from having bilayers and then summarize the resulting impact on the exciton energy landscape from these effects (paper I.). For this purpose we will start in the monolayer basis and add the specific bilayer effects on top of that. The two effects that will change the monolayer exciton bandstructure due to the presence of another layer are interlayer hybridization and the polarization-induced alignment shift. In twisted structures these components are what makes up the moiré potential.

Before we go into detail about these modifications to the Hamiltonian we must first consider the new exciton species that arise by having a bilayer TMD. Here we do not only have excitons confined to one layer, but also interlayer excitons where the electron and hole are spatially separated in different layers [14, 18, 50, 51] (as illustrated in Fig 1.2). Consequently, we have to adjust the screening when solving the Wannier equation (Eq. 2.26). This was done in Ref. [52] by Simon Ovesen et al. and this generalized

screening reads

$$
\epsilon_{scr}^{ll'}(\boldsymbol{q}) = \begin{cases} \epsilon_{inter}(\boldsymbol{q}), & l \neq l' \\ \epsilon_{intra}^{l}(\boldsymbol{q}), & l = l' \end{cases} ,
$$

$$
\epsilon_{inter}(\boldsymbol{q}) = \kappa_{sub} g_{\boldsymbol{q}}^{0} g_{\boldsymbol{q}}^{1} f_{\boldsymbol{q}}, \quad \epsilon_{intra}^{l}(\boldsymbol{q}) = \frac{\kappa_{sub} g_{\boldsymbol{q}}^{1-l} f_{\boldsymbol{q}}}{\cosh(\delta_{1-l}\boldsymbol{q}/2) h_{\boldsymbol{q}}^{l}}.
$$

(3.1)

Here, we use the abbreviations

$$
\begin{aligned}
f_{\boldsymbol{q}} &= 1 + \frac{1}{2}\Big[(\frac{\kappa_0}{\kappa_{sub}} + \frac{\kappa_{sub}}{\kappa_0})\tanh(\delta_0\boldsymbol{q}) + (\frac{\kappa_1}{\kappa_{sub}} + \frac{\kappa_{sub}}{\kappa_1})\tanh(\delta_1\boldsymbol{q}) \\
&+ (\frac{\kappa_0}{\kappa_1} + \frac{\kappa_1}{\kappa_0})\tanh(d_0\boldsymbol{q})\tanh(\delta_1\boldsymbol{q})\Big], \\
h_{\boldsymbol{q}}^{l} &= 1 + \frac{\kappa_{sub}}{\kappa_l}\tanh(\delta_l\boldsymbol{q}) + \frac{\kappa_{sub}}{\kappa_{1-l}}\tanh(\delta_{1-l}\boldsymbol{q}/2) \\
&+ \frac{\kappa_l}{\kappa_{1-l}}\tanh(\delta_l\boldsymbol{q})\tanh(\delta_{1-l}\boldsymbol{q}/2), \\
g_{\boldsymbol{q}}^{l} &= \frac{\cosh(\delta_l\boldsymbol{q})}{\cosh(\delta_{1-l}\boldsymbol{q}/2)[1 + \frac{\kappa_{sub}}{\kappa_l}\tanh(\delta_l\boldsymbol{q}/2)]},
\end{aligned}
$$

(3.2)

where κ_{sub} is the dielectric components of the substrate as the defined in Eq. 2.12 and κ_l is instead for TMD layer indexed with l (i.e $l = (0,1)$). Here, $\delta_l = \alpha_l d_l$, where d_l is the layer thickness of the TMD and α_l also is defined in Eq. 2.12. The dielectric components and the layer thicknesses are obtained from Ref. [53]. The above screening can be derived by solving the Poisson equation for two dielectric media on top of each other. With this generalized screening formula we can calculate the decoupled binding energies for both intra- and interlayer excitons.

3.1 Polarization-induced alignment shift

The first effect we wish to take into account is the polarization-induced alignment shift, sometimes also refereed to as ferroelectric potential [54]. This alignment shift stems from the polarization between the atoms of the different layers, in turn inducing an electrostatic potential that will shift the exciton bandstructure [24, 28, 55–57]. It is then intuitive to understand that
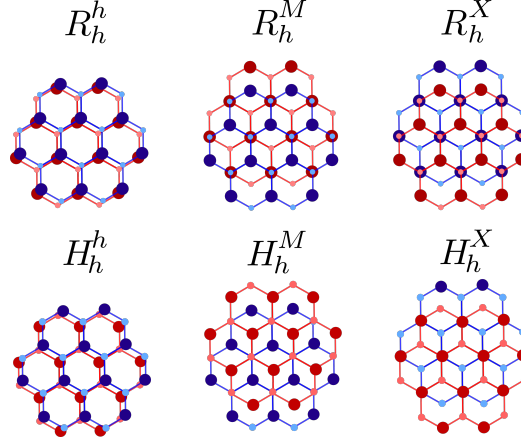
Figure 3.1: Schematic for the different high symmetry stackings found in bilayer TMDs.

the interlayer excitons, which harbor an out-of-plane dipole moment, will be the exciton that is strongly affected by this shift.

Since the polarization is directly dependent on the atomic configuration, this energy renormalization of the exciton bandstructure change with different stackings. In bilayer TMDs we have two fundamentally different stackings, each with three high symmetry stackings (cf. Fig 3.1), thus we will need to calculate this shift for all stacking configurations.

The matrix elements governing the polarization-induced alignment shift of the single particle states are given by

$$\Delta\varepsilon_l^{\alpha\mathbf{k}} = \int d\mathbf{r}\, n_{l,\alpha\mathbf{k}}(\mathbf{r})\delta V_{\mathrm{pol}}(\mathbf{r}). \tag{3.3}$$

They were computed via *ab inito* calculations by Christopher Linderälv in paper I., where $n_{l,\alpha\mathbf{k}}$ is the orbital density of state $|\alpha\mathbf{k}\rangle$ of monolayer l. Here, $\alpha = (\lambda,\xi)$ is a compound index, where $\lambda = (c,v)$ is the band index and ξ is the valley index. To this end, δV_{pol} is the solution to the Poisson equation for the electron density difference δn ($\nabla^2\delta V_{\mathrm{pol}} - \delta n = 0$) with $\delta n = n_{1,2} - n_1 - n_2$, with the subscript indicating the layer. By calculating this for each stacking one can add a stacking dependent renormalization to the kinetic energy part of the exciton Hamiltonian, i.e $\tilde{E}_{l\mathbf{k}}^\alpha(S) = E_{l\mathbf{k}}^\alpha + \Delta\varepsilon_l^\lambda(S)$. Furthermore, we can calculate the intermediate displacements by interpolating these values with

23

a continuous fit function given by Ref. [28],

$$\tilde{E}_l^\lambda(S) = \mathcal{E}_l^\lambda + \left(\alpha_l^\lambda + \beta_l^\lambda e^{\frac{2\pi i \sigma_{1-l}}{3}} \right) \sum_{n=0}^{2} e^{i C_3^{(n)} \boldsymbol{G}_l \cdot \boldsymbol{D}_l(S)}, \tag{3.4}$$

where $\mathcal{E}_l^\lambda$ is the stacking-independent monolayer energy and $\sigma_l = (-1)^l$ for H-type stacking, otherwise $\sigma_l = 1$. Here, $C_3^{(n)}$ is the three fold rotation operator acting upon the reciprocal lattice vector $\boldsymbol{G}_l$. The displacement vector between the two layers are given by $\boldsymbol{D}_l(S)$, where S is the stacking. Furthermore, α_l^λ and β_l^λ determine the stacking-dependent shift. These parameters are fitted to the band structure for the K point, obtained from first-principle calculations $\tilde{E}_{l\mathbf{0}}^{\lambda K}(S) = E_{l\mathbf{0}}^\alpha + \Delta \varepsilon_l^\lambda(S)$, where the momentum is $\boldsymbol{k} = \mathbf{0}$, i.e the minimum of the parabolic dispersion. For the correct energetic position of other valleys, one has to take into account the spectral valley separation and spin orbit splitting which can be found in Ref. [35].

3.2 Exciton hybridization

The second modification to the monolayer band energies we need to take into account is the interlayer tunneling. Here, the overlapping electron wavefunctions between the layers allows for the carriers to tunnel and thus form hybridized exciton states, i.e a mixture between an interlayer exciton and an intralayer exciton [29, 58–60]. A schematic illustration of this can be seen in Fig 3.2.a and Fig 3.2.b, where the example heterostructure MoS_2-WS_2 displays strong hybridization around the ΓK exciton. Since the overlap between the wavefunctions strongly depends on the interlayer distance, this modification to the monolayer energy is also stacking dependent, thus leaving us with a stacking dependent tunneling matrix element $T_{ll'}^\alpha(S)$.

Starting in electron/hole basis we first consider the tunneling around the K point. Here, the conduction and valence band Bloch waves are composed out of d-orbitals [29, 61, 62]. Using the angular symmetry of d-orbitals, the tunneling around the three equivalent K points in an untwisted structure can be written as [29]

$$T_{ll'}^\alpha(S) = \sum_{n=0}^{2} t^\alpha(S) \, e^{i\tau (C_3^{(n)} \boldsymbol{K} - \boldsymbol{K}) \cdot \boldsymbol{D}(S)}, \tag{3.5}$$

where $C_3^{(n)}$ again denotes the three-fold rotation operator and $\boldsymbol{D}(S)$ the stacking dependent lateral displacement between the layers. Furthermore, $t^\alpha(S)$ describes the tunneling strength and τ is a prefactor which equals 1 for the K and -1 for the K$'$ point. For H-type structures, this expression obtains the additional phase $e^{i(-1)^{l'}2\pi/3}$ for the valance band [29].

Due to the C$_3$-symmetry, tunneling can only occur for certain stacking configurations. To demonstrate this effect, we first consider tunneling around the K point for R-type structures and apply the corresponding lateral displacement vectors $\boldsymbol{D}(S)$ for each high-symmetry stacking. We find that the tunneling term vanishes for R_h^M and R_h^X around the K point [63]. For an H-type structure one of the two layers is inverted (rotated by $180°$) relative to the R-structure. Here, the tunneling for both electrons and holes vanishes at H_h^M. In addition, hole (electron) tunneling does not occur at H_h^X (H_h^h). This means that we only have a non-zero tunneling matrix element at the K point for R_h^h, H_h^X (electron tunneling) and H_h^h (hole tunneling) stacking. In these cases, Equation 3.5 simply becomes $T_{ll'}^\alpha(S) = 3t^\alpha(S)$. With the factor 3 reflecting the three equivalent K points.

For tunneling around the Γ and Λ points, there are no equivalent points within the first Brillouin zone (BZ) and thus the tunneling matrix element is only given by the tunneling strength $T_{ll'}^\alpha(S) = t^\alpha(S)$ [29]. This tunneling strength can be extracted from DFT calculations of the bilayer band structure by considering the Hamiltonian in electron/hole basis

$$H = \sum_{\alpha l \boldsymbol{k}} \tilde{E}_{l\boldsymbol{k}}^\alpha(S)\, a_{\alpha l \boldsymbol{k}}^\dagger a_{\alpha l \boldsymbol{k}} + \sum_{\substack{\alpha \boldsymbol{k} \\ l \neq l'}} T_{ll'}^\alpha(S)\, a_{\alpha l \boldsymbol{k}}^\dagger a_{\alpha l' \boldsymbol{k}}, \tag{3.6}$$

where l/l' are layer indices while $\alpha = (\lambda,\xi)$ is a compound index with ξ denoting the valley and $\lambda = (c,v)$ the conduction and the valence band, respectively. This can be thought off as a 2×2 matrix with respect to the layer index l/l'. Here, the diagonal components are given by $\tilde{E}_{l\boldsymbol{k}}^\alpha(S)$ and the off-diagonal terms correspond to the tunneling $T_{ll'}^\alpha(S)$. The eigenvalues of this matrix are given by the avoided-crossing formula

$$\mathcal{E}_{\pm,\boldsymbol{k}}^\alpha(S) = \frac{1}{2}\sum_{l=1}^{2} \widetilde{E}_{l\boldsymbol{k}}^\alpha(S) \pm \frac{1}{2}\sqrt{\widetilde{\Delta}_{\boldsymbol{k}}^\alpha(S)^2 + 4|t^\alpha(S)|^2}, \tag{3.7}$$

where $\widetilde{\Delta}_{\boldsymbol{k}}^\alpha(S) = \widetilde{E}_{1\boldsymbol{k}}^\alpha(S) - \widetilde{E}_{2\boldsymbol{k}}^\alpha(S)$ is the spectral difference between the
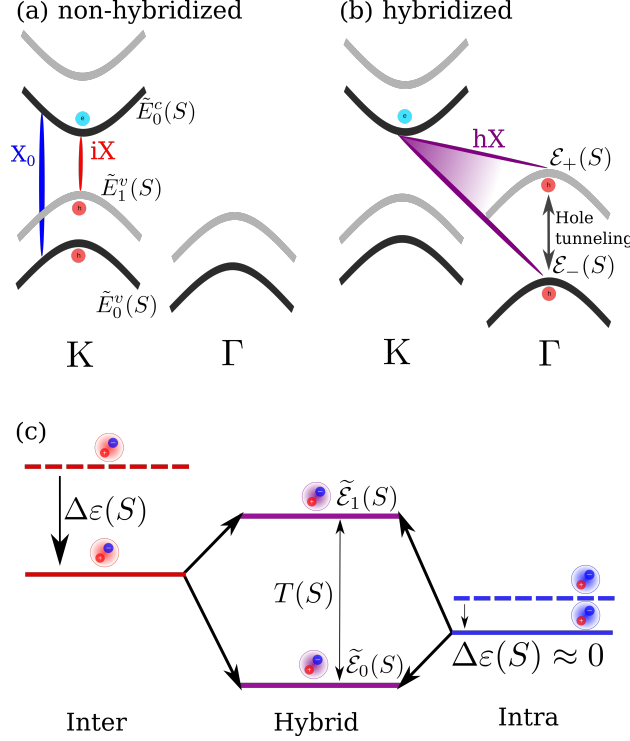
Figure 3.2: (**a**) Schematic of the electronic band structure in MoS_2(black)-WS_2(gray) heterostructure (a) before and (b) after hybridization. The intralayer (X_0) and interlayer (iX) excitons are marked in blue and red, respectively. The strong tunneling of holes around the Γ point results in a pronounced hybrid exciton state (hX, purple line). (**c**) Schematic for the formation of hybrid excitons. The dashed lines are the unperturbed exciton energies that become shifted by $\Delta\varepsilon(S)$ due to the layer polarization. Interlayer hybridization results in hybrid exciton states denoted by $\widetilde{\mathcal{E}}_\eta(S)$.

monolayer energies as extracted from DFT calculations shifted by the layer polarization-induced alignment potential (see section 3.1). Furthermore, $|t^\alpha(S)|$ is the tunneling strength (see Equation 3.5) and $\mathcal{E}^\alpha_{\pm,\mathbf{k}}(S)$ are the hybrid energies corresponding to the bilayer eigenenergies extracted from DFT calculations. Exploiting Equation 3.7, the tunneling strength can be calculated for each band, valley, and stacking, yielding

$$|t^\alpha(S)| = \frac{1}{2}\sqrt{(\Delta\mathcal{E}^\alpha_{\mathbf{k}}(S))^2 - \widetilde{\Delta}(S)^2}, \qquad (3.8)$$

where $\Delta\mathcal{E}^\alpha_{\mathbf{k}}(S) = \mathcal{E}^\alpha_{+,\mathbf{k}}(S) - \mathcal{E}^\alpha_{-,\mathbf{k}}(S)$ is the spectral difference between the
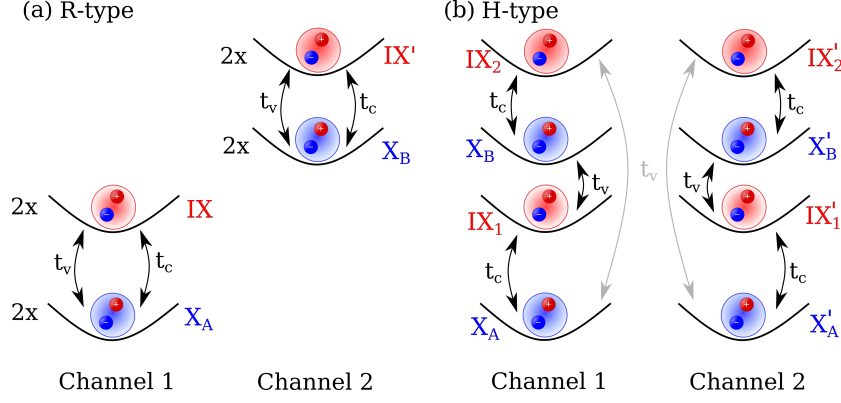
Figure 3.3: Schematic for the different tunneling channels in R-type structures **(a)** and H-type structures **(b)**. Here, 2x notes that the exciton state is two-fold degenerate. In H-type structures K' is on top of K thus creating fundamentally different tunneling channels. This allows for the lowest lying interlayer exciton to hybridize with the B exciton.

hybridized electronic states.

Applying the exciton transformation from subsection 2.3.2 to the Hamiltonian in Eq. 3.6 we find that the tunneling matrix element reads in exciton basis

$$
\begin{aligned}
T^{\xi}_{LL'}(S) = \mathcal{F}^{\xi}_{LL'}(T^{c\xi_e}_{l_e l'_e}(S)\delta_{l_e, l'_e - 1}\delta_{l_h, l'_h} \\
- T^{v\xi_h}_{l_h l'_h}(S)\delta_{l_h, l'_h - 1}\delta_{l_e, l'_e}),
\end{aligned}
\tag{3.9}
$$

where $L = (l_e, l_h)$ is a compound layer index and the deltas are there to ensure that we only have a single carrier to tunnel at a single time. Here, $\mathcal{F}^{\xi}_{LL'}$ are the exciton formfactors which reads

$$
\mathcal{F}^{\xi}_{LL'} = \sum_{\boldsymbol{k}} \Psi^{*}_{\xi L}(\boldsymbol{k})\Psi_{\xi L'}(\boldsymbol{k}),
\tag{3.10}
$$

where $\Psi_{\xi L}(\boldsymbol{k})$ are the exciton wavefunctions as obtained from the generalized Wannier equation (Eq. 2.26 and Eq. 3.1). An illustration of the hybridization process that then occur for excitons can be seen in Fig 3.2.c. Here, the decoupled monolayer energies of the interlayer and intralayer exciton is shifted by the alignment shift which is then split into two hybrid exciton states. It is important to note here that the tunneling channel for which

intralayer excitons and interlayer exciton couple to each other change drastically with stacking. If we consider a homobilayer at R_h^h stacking we will have two degenerate intralayer excitons (one for each layer) and two degenerate interlayer excitons ($l_e = 0, l_h = 1$ and $l_e = 1, l_h = 0$) that couple to each other via carrier tunneling (cf. Fig 3.3.a).

Normally we only think of the KK exciton, also known as the A exciton, but we also have the B exciton (K'K'). Due to the large spin-orbit coupling in TMDs these excitons are very far up in energy and can thus be neglected usually, which is the case in R-type structures (see X_B and IX' in Fig 3.3.a). However, in H-type structures the K' point lie above the K point of the other layer. This breaks the degeneracy of the excitons with respect to the tunneling channel and now the A exciton couples to the B exciton. Consequently, we have a new set of interlayer excitons that in turn can hybridize with the B exciton (cf. Fig 3.3.b).

3.3 Energetic landscape

Taking into account the two bilayer modifications to the monolayer energy we have discussed, the exciton Hamiltonian then reads

$$H = \sum_{\substack{\xi \boldsymbol{Q} \\ LL'}} (E_{L\boldsymbol{Q}}^{\xi}(S) X_{L\boldsymbol{Q}}^{\xi\dagger} X_{L\boldsymbol{Q}}^{\xi} \delta_{LL'} + T_{LL'}^{\xi}(S) X_{L\boldsymbol{Q}}^{\xi\dagger} X_{L'\boldsymbol{Q}}^{\xi}),$$

(3.11)

where $E_{L\boldsymbol{Q}}^{\xi}(S)$ takes into account the energies of the excitons, the relative valley position and the polarization induced alignment shift. Here, $T_{LL'}^{\xi}(S)$ is the tunneling matrix element as discussed in the previous section. We now wish to find a diagonal form of this Hamiltonian. For this purpose we expand the exciton operator into a hybrid exciton basis [28, 29]

$$Y_{\xi\eta\boldsymbol{Q}}^{\dagger} = \sum_{L} \mathcal{C}_L^{\xi\eta*}(\boldsymbol{Q}) X_{L\boldsymbol{Q}}^{\xi\dagger},$$

(3.12)

where η is the new hybrid exciton quantum number, $Y_{\xi\eta\boldsymbol{Q}}^{\dagger}$ are the hybrid exciton operators and $\mathcal{C}_L^{\xi\eta}(\boldsymbol{Q})$ are the mixing coefficients revealing the relative contribution between intra/interlayer exciton states. Since the mixing
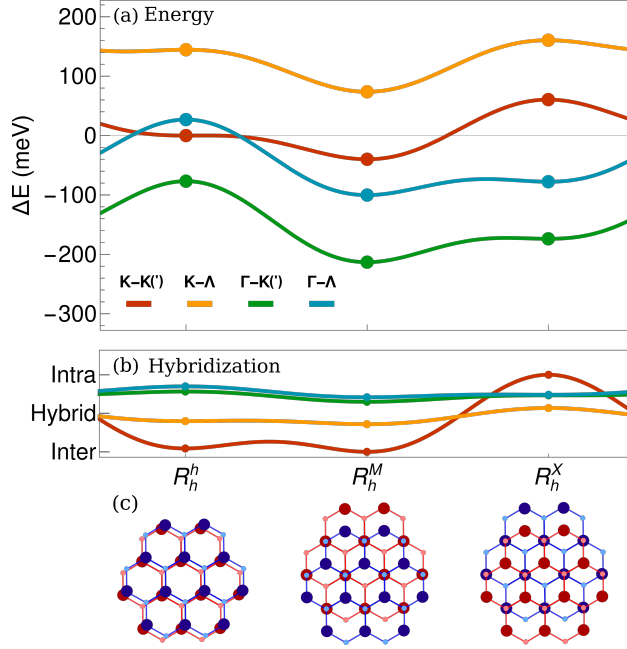
Figure 3.4: (**a**) Lowest lying exciton state for each exciton valley configuration as a function of stacking for the MoS_2-WS_2 heterostructures on a SiO_2 substrate. All energies are expressed in relation to the bright K-K exciton at R_h^h. Note that K-K and K-K′ as well as Γ-K and Γ-K′ are almost degenerate. (**b**) Degree of hybridization for each exciton valley as a function of stacking. (**c**) Schematic for R-type stacking configurations, where blue indicates the WS_2 and red the MoS_2 layer.

coefficients are eigenvectors to the Hamiltonian they fulfill the following requirements

$$\sum_L \mathcal{C}_L^{\boldsymbol{\xi}\eta_1*}(\boldsymbol{Q})\mathcal{C}_L^{\boldsymbol{\xi}\eta_2}(\boldsymbol{Q}) = \delta_{\eta_1\eta_2}$$
$$\sum_\eta \mathcal{C}_L^{\boldsymbol{\xi}\eta*}(\boldsymbol{Q})\mathcal{C}_{L'}^{\boldsymbol{\xi}\eta}(\boldsymbol{Q}) = \delta_{LL'}. \tag{3.13}$$

Applying the following transformation to the exciton Hamiltonian gives us the hybrid exciton eigenvalue equation

$$E_{L\boldsymbol{Q}}^\xi(S)\mathcal{C}_{L\boldsymbol{Q}}^{\xi\eta} + \sum_{L'} T_{LL'}^\xi(S)\mathcal{C}_{L'\boldsymbol{Q}}^{\xi\eta} = \mathcal{E}_{\eta\boldsymbol{Q}}^\xi(S)\mathcal{C}_{L\boldsymbol{Q}}^{\xi\eta}. \tag{3.14}$$

29

Here, $\mathcal{E}_{\eta\boldsymbol{Q}}^{\xi}(S)$ are the the final hybrid exciton energies. Solving this numerically, which is the equivalent of diagonalizing a 4×4 matrix, we obtain the diagonal form of the interaction free bilayer exciton Hamiltonian.

$$H_0 = \sum_{\boldsymbol{Q\xi}\eta} \mathcal{E}_{\eta\boldsymbol{Q}}^{\boldsymbol{\xi}}(S) Y_{\boldsymbol{\xi}\eta\boldsymbol{Q}}^{\dagger} Y_{\boldsymbol{\xi}\eta\boldsymbol{Q}}. \tag{3.15}$$

This was done for the van der Waals heterostructure MoS_2-WS_2 in paper I. for different R-type stackings and valleys. The resulting exciton bandstructure is shown in Fig 3.4.a, where the lowest lying exciton for each valley is shown as a function of stacking (cf. Fig 3.4.c). Here we can see the strong impact of the carrier tunneling, consequently making the ΓK exciton the lowest lying one. The variation in energy between different stackings can mainly be explained by the varying interlayer distance, which in turn heavily impacts the tunneling strength. In Fig 3.4.b we see how the degree of hybridization changes with stacking, revealing a very small change for the momentum dark excitons. Interestingly, we find that the intralayer KK exciton no longer is the lowest lying one when going between R_h^M to R_h^X. Here, the alignment shift blueshifts this exciton sufficiently for the low lying interlayer exciton to become the lowest lying one.

3.4 Optical response

Now when we have access to the hybrid exciton energy landscape we wish to know what the corresponding optical response is. In the example material used here (MoS_2-WS_2), the momentum dark excitons are by far the lowest. Consequently, this exciton energy landscape is not directly accessible via optical absorption or via direct emission of a photon. Instead, the exciton will first need to scatter with a phonon to virtual bright state and then emit a photon. This phonon-assisted recombination of said exciton will then result in multiple phonon sidebands emerging from the scattering process, in turn giving us the optical response of the material via the photoluminescence (PL) spectra. This phonon-assisted PL formula was first derived by Samuel Brem et al. in Ref. [64] and then later generalized to bilayers in Ref. [29]. More information concerning the exact expression for this phonon-assisted PL can be found in the appended papers as well (paper I.,II.).
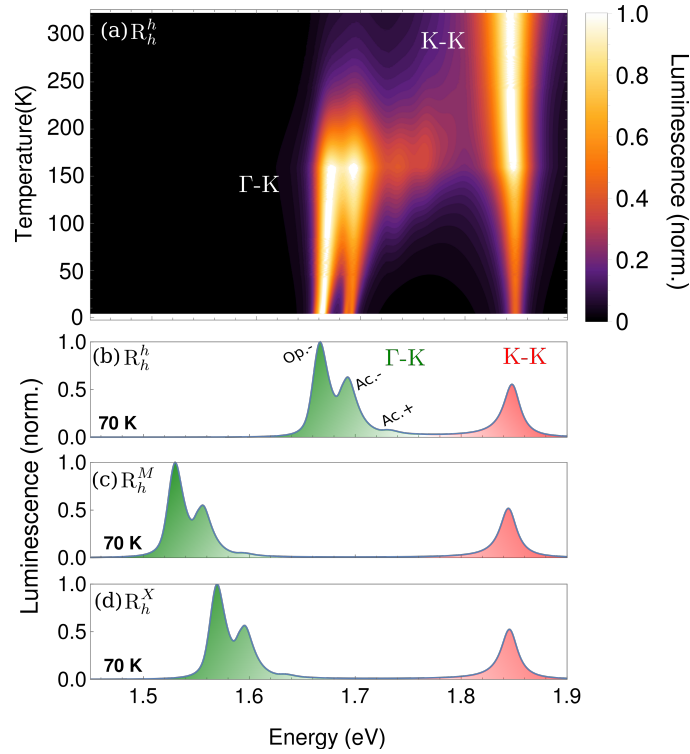
Figure 3.5: **(a)** Normalized photoluminescence spectra as a function of temperature and energy for R_h^h-stacking in the MoS$_2$-WS$_2$ heterostructure. PL spectra at 70 K for **(b)** R_h^h, **(c)** R_h^M and **(d)** R_h^X stacking. The green and the red shaded areas indicate the phonon sidebands of the Γ-K exciton and the K-K intralayer exciton, respectively. Phonon sidebands stemming from emission (−) and absorption (+) of optical (Op) and acoustical (Ac) phonons are labeled accordingly.

The phonon-assisted PL was calculated in Fig 3.5.a for R_h^h stacking, corresponding to the hybrid exciton bandstructure shown in Fig 3.4. Here, one can see the the clear domination of the phonon-assisted PL peaks at low temperatures and at higher temperatures the KK exciton will again dominate the spectrum. This is due to the Boltzmann nature of the exciton distribution[1], where the direct emission, which corresponds to the leading order term, will gain a larger occupation. This in turn will affect the PL intensity for said peaks. At the lower temperatures the process of emitting

---

[1]The exciton distribution will in reality follow a Bose-Einstein distribution, but can be well approximated as a Boltzmann distribution at low densities [29, 64].

a phonon is the dominating one. This is due to the number of phonons scaling with temperature. In the intermediate temperature range, we can see phonon absorption appearing as well. Furthermore, we can see the clear splitting between the optical and acoustical phonon modes since these will not have the same phonon energies [36, 41]. The hybrid exciton energies have then been redshifted(blueshifted) with these phonon energies, which then determines the relative position to A exciton (KK) peak[2]. This peak is in turn fitted to experimental observations since calculating the absolute PL peak position would require reliable first principle calculations concerning the band gap. For the purpose of this PL calculation, the linewidth has been phenomenologically modeled in accordance with Ref. [67].

Looking at Fig 3.5.a to Fig 3.5.c we see the how this optical response varies with stacking, again reflecting the strong variation of tunneling strength due to the changing interlayer distance. The above calculated results are in good agreement with experimental findings, where two predicted phonon sidebands have been observed about 300 meV below the bright K-K exciton in MoS_2-WS_2 [68]. This corresponds well to the calculated PL at R_h^M- and R_h^X-stacking, which is the energetically most favorable R-type stackings.

---

[2]Additional energy renormalizations will appear due to exciton-exciton interactions, but since these only become significant at higher densities they have been neglected here [65, 66].

CHAPTER **4**

EXTERNAL TUNING OF MOIRÉ EXCITONS

In the previous chapter we summarized the results from paper I. where the hybrid exciton landscape was modeled, taking into account the bilayer modifications to the monolayer exciton energies. In this chapter we will investigate how one can exploit these insights in order to externally tune the optical response of the material. We do this by studying the interplay between twist angle engineering and applied electrical fields. This chapter consequently summarizes the theory and results from paper II..

4.1   Generalizing to moiré exciton Hamiltonian

The first thing we need to do is generalize our exciton Hamiltonian for the inclusion of twist angles. Since both the polarization-induced alignment shift and the tunneling is dependent on the atomic configuration these will be periodic in real space (cf. Fig 4.1). Our aim is then to generalize the model so that it will incorporate these periodic features over the whole superlattice.

This is done by starting with a real space representation of the two bilayer
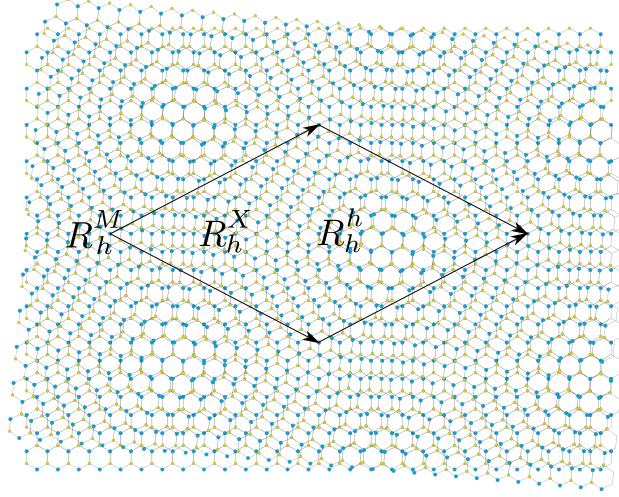
Figure 4.1: Schematic of a twisted bilayer TMD superlattice.

modifications to the exciton landscape. Both of these effects are what consti-
tutes the moiré potential [56] and we will thus call the combined Hamiltonian
the moiré Hamiltonian. In electron-hole basis this reads

$$H_M = \sum_{i\lambda \boldsymbol{r}} V_{ii}^{\lambda}(\boldsymbol{r})\Psi_i^{\lambda\dagger}(\boldsymbol{r})\Psi_i^{\lambda}(\boldsymbol{r}) + \sum_{\substack{i\neq j \\ \lambda \boldsymbol{r}}} T_{ij}^{\lambda}(\boldsymbol{r})\Psi_i^{\lambda\dagger}(\boldsymbol{r})\Psi_j^{\lambda}(\boldsymbol{r}) + h.c. \qquad (4.1)$$

Here, $i(j) = (l,\xi)$ is a compound index, $\boldsymbol{r}$ is the real space coordinate in the
superlattice and $\Psi^{(\dagger)}$ are annihilation(creation) operators. The first term ac-
counts for the periodic alignment shift (section 3.1) and the second term
accounts for the interlayer tunneling (section 3.2). We can approximate
the wavefunctions in the vicinity of high symmetry points as plane waves
$\Psi_i^{\lambda\dagger}(\boldsymbol{r}) = \sum_{\boldsymbol{k}} e^{i\boldsymbol{k}\cdot\boldsymbol{r}}\lambda_{i,\boldsymbol{k}}^{\dagger}$ due to the effective mass approximation made in 2.2.3.
This is analogous to Fourier transforming the Hamiltonian to momentum
space

$$H_M = \sum_{\substack{i\lambda \\ \boldsymbol{kg}}} v_{ii}^{\lambda}(\boldsymbol{g})\lambda_{i,\boldsymbol{k}+\boldsymbol{g}}^{\dagger}\lambda_{i,\boldsymbol{k}} + \sum_{\substack{i\neq j\lambda \\ \boldsymbol{gkq}}} t_{ij}^{\lambda}(\boldsymbol{g})\lambda_{i,\boldsymbol{k}+\boldsymbol{g}}^{\dagger}\lambda_{j,\boldsymbol{k}} + h.c, \qquad (4.2)$$

where $\boldsymbol{g}$ are the reprical lattice vectors of the mini Brillouin zone (mBZ)
that emerges due to the real space superlattice (cf. Fig 4.2). This vector is
consequently defined as $\boldsymbol{g} = \boldsymbol{G}_1 - \boldsymbol{G}_2$, where $\boldsymbol{G}_l$ are the reciprocal lattice
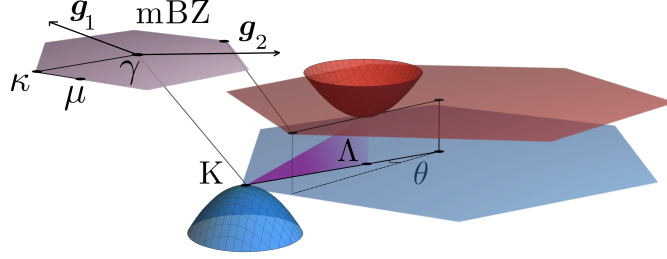
Figure 4.2: Schematic of the mini Brillouin zone that emerges due to the emergence of a real space superlattice and a schematic interpretation of the hybrid moiré excitons that will be heavily affected by the twist angle.

vector of layer l. The above equation is obtained by expanding the periodic moiré potential as a Fourier series

$$V_{ii}^{\lambda}(\boldsymbol{r}) = \sum_{\boldsymbol{g}} v_{ii}^{\lambda}(\boldsymbol{g})e^{i\boldsymbol{g}\cdot\boldsymbol{r}}. \tag{4.3}$$

Here, the mBZ lattice vectors $\boldsymbol{g}$ are the eigenmodes of this expansion. Consequently, the matrix elements in Eq. 4.2 are simply the Fourier coefficients of this expansion and can be obtained by solving the following integral

$$v_{ii}^{\lambda}(\boldsymbol{g}) = \frac{1}{\mathcal{A}_{\mathrm{M}}} \int_{\mathcal{A}_{\mathrm{M}}} d\boldsymbol{r} e^{-i\boldsymbol{g}\cdot\boldsymbol{r}} V_{ii}^{\lambda}(\boldsymbol{r}), \tag{4.4}$$

where $\mathcal{A}_{\mathrm{M}}$ is the unit area of the superlattice. Here, the polarization-induced alignment shift is used an example, but the same approach is done for the tunneling as well.

With the above approach we only need to know how the moiré potential looks in real space. Assuming a rigid lattice model (i.e the lattice constant remains the same as in the monolayer case) we can smoothly interpolate between the high symmetry stackings. Since these values were previously obtained for both the tunneling and the alignment shift in chapter 3 (paper I.) this becomes a simple question of using a similar scheme as in Eq. 3.4 in order to obtain the intermediate moiré potential landscape [28].

$$V_{ii}^{\lambda}(\boldsymbol{r}) = \mathrm{Re}\left[v_i^{\lambda} + (\mathcal{A}_i^{\lambda} + \mathcal{B}^{\lambda}e^{i2\pi/3})\sum_{n=0}^{2}e^{i\boldsymbol{g}_n\cdot\boldsymbol{r}}\right], \tag{4.5}$$

35

where v_i^λ, $\mathcal{A}_i^\lambda$ and $\mathcal{B}^\lambda$ are the parameters which we fit to the known alignment shifts/tunneling strengths.

Applying the exciton transformation from subsection 2.3.2 we can now write down the complete interaction-free exciton Hamiltonian

$$
\begin{aligned}
H_0 &= \sum_{LQ\boldsymbol{\xi}} E_{LQ}^{\boldsymbol{\xi}} X_{L,Q}^{\boldsymbol{\xi}\dagger} X_{L,Q}^{\boldsymbol{\xi}} + \sum_{\substack{LQ\boldsymbol{\xi} \\ \boldsymbol{g}}} V_L^{\boldsymbol{\xi}}(\boldsymbol{g}) X_{L,Q+g}^{\boldsymbol{\xi}\dagger} X_{L,Q}^{\boldsymbol{\xi}} \\
&+ \sum_{\substack{LL' \\ Q\boldsymbol{\xi}\boldsymbol{g}}} T_{LL'}^{\boldsymbol{\xi}}(\boldsymbol{g}) X_{L,Q+g}^{\boldsymbol{\xi}\dagger} X_{L',Q}^{\boldsymbol{\xi}} + h.c,
\end{aligned}
\tag{4.6}
$$

Here, the first term accounts for the dispersion

$$
E_{LQ}^{\boldsymbol{\xi}} = \hbar^2 \frac{(\boldsymbol{Q} - [\xi_e - \xi_h])^2}{2[m_e + m_h]} + \varepsilon_{\xi_e 0}^c - \varepsilon_{\xi_h 0}^v + E_{\boldsymbol{\xi}}^{\mathrm{b}},
\tag{4.7}
$$

where $E_{\boldsymbol{\xi}}^{\mathrm{b}}$ are the exciton binding energies and $\varepsilon_{\boldsymbol{\xi}_\lambda}^\lambda$ is the valley splitting (Ref. [35]).

The matrix element of the polarization-induced alignment shift is given by

$$
V_L^{\boldsymbol{\xi}}(\boldsymbol{g}) = v_{l_e}^c(\boldsymbol{g}) \mathcal{F}_{LL}^{\boldsymbol{\xi}}(\beta_{LL}\boldsymbol{g}) - v_{l_h}^v(\boldsymbol{g}) \mathcal{F}_{LL}^{\boldsymbol{\xi}*}(-\alpha_{LL}\boldsymbol{g}),
\tag{4.8}
$$

where $v_{l_\lambda}^\lambda(\boldsymbol{g})$ are the Fourier coefficients as obtained from Equation 4.4 and $\mathcal{F}_{LL'}^{\boldsymbol{\xi}}(\boldsymbol{q})$ are the form factors given by

$$
\mathcal{F}_{LL'}^{\boldsymbol{\xi}}(\boldsymbol{q}) = \sum_{\boldsymbol{k}} \Psi_L^{\boldsymbol{\xi}*}(\boldsymbol{k}) \Psi_{L'}^{\boldsymbol{\xi}}(\boldsymbol{k} + \boldsymbol{q}).
\tag{4.9}
$$

The tunneling matrix element is similarly given by

$$
\begin{aligned}
T_{LL'}^{\boldsymbol{\xi}}(\boldsymbol{g}) = \Big[& \delta_{l_h, l_h'} (1 - \delta_{l_e, l_e'}) t_{l_e l_e'}^{c\boldsymbol{\xi}_e}(\boldsymbol{g}) \mathcal{F}_{LL'}^{\boldsymbol{\xi}}(\beta_{LL'}\boldsymbol{g}) \\
& - \delta_{l_e, l_e'} (1 - \delta_{l_h, l_h'}) t_{l_h l_h'}^{v\boldsymbol{\xi}_h}(\boldsymbol{g}) \mathcal{F}_{LL'}^{*\boldsymbol{\xi}}(-\alpha_{LL'}\boldsymbol{g}) \Big],
\end{aligned}
\tag{4.10}
$$

where the delta functions ensure that only an electron or hole can tunnel at the same time and $t_{l_\lambda l_{\lambda'}}^{\lambda\boldsymbol{\xi}_\lambda}(\boldsymbol{g})$ are the Fourier coefficients of the real space tunneling landscape, in analogy to Equation 4.4.

In a similar fashion as in chapter 3 we want to find a diagonal form for the Hamiltonian in Eq. 4.6. Before we can to this we must first deal with the additional periodicity of the superlattice. This is done by considering the well known zone folding scheme. Here, we restrict our summation over the center-of-mass momentum $\boldsymbol{Q}$ to the mBZ and then fold the dispersion back in again with the mBZ lattice vectors $\boldsymbol{g}$ [28, 29].

$$
\begin{aligned}
H_0 &= \sum_{\substack{LQ\boldsymbol{\xi} \\ \boldsymbol{g}}} E_{L\boldsymbol{Q}}^{\boldsymbol{\xi}}(\boldsymbol{g}) X_{L,\boldsymbol{Q}+\boldsymbol{g}}^{\boldsymbol{\xi}\dagger} X_{L,\boldsymbol{Q}+\boldsymbol{g}}^{\boldsymbol{\xi}} + \sum_{\substack{LQ\boldsymbol{\xi} \\ \boldsymbol{gg}'}} V_L^{\boldsymbol{\xi}}(\boldsymbol{g}') X_{L,\boldsymbol{Q}+\boldsymbol{g}+\boldsymbol{g}'}^{\boldsymbol{\xi}\dagger} X_{L,\boldsymbol{Q}+\boldsymbol{g}}^{\boldsymbol{\xi}} \\
&+ \sum_{\substack{LL'\boldsymbol{Q} \\ \boldsymbol{\xi gg}'}} T_{LL'}^{\boldsymbol{\xi}}(\boldsymbol{g}') X_{L',\boldsymbol{Q}+\boldsymbol{g}+\boldsymbol{g}'}^{\boldsymbol{\xi}\dagger} X_{L,\boldsymbol{Q}+\boldsymbol{g}}^{\boldsymbol{\xi}} + h.c,
\end{aligned}
\tag{4.11}
$$

where $E_{L\boldsymbol{Q}}^{\boldsymbol{\xi}}(\boldsymbol{g}) = E_{L\boldsymbol{Q}+\boldsymbol{g}}^{\boldsymbol{\xi}}$ and the summation over $\boldsymbol{Q} \in$ mBZ. We simplify the above expression by introducing the zone-folding operators $F_{L\boldsymbol{Q}\boldsymbol{g}}^{\boldsymbol{\xi}} = X_{L,\boldsymbol{Q}+\boldsymbol{g}}^{\boldsymbol{\xi}}$ and apply them to the Hamiltonian

$$
\begin{aligned}
H_0 &= \sum_{\substack{LQ\boldsymbol{\xi} \\ \boldsymbol{g}}} E_{L\boldsymbol{Q}}^{\boldsymbol{\xi}}(\boldsymbol{g}) F_{L\boldsymbol{Q}\boldsymbol{g}}^{\boldsymbol{\xi}\dagger} F_{L\boldsymbol{Q}\boldsymbol{g}}^{\boldsymbol{\xi}} + \sum_{\substack{LQ\boldsymbol{\xi} \\ \boldsymbol{gg}'}} V_L^{\boldsymbol{\xi}}(\boldsymbol{g},\boldsymbol{g}') F_{L\boldsymbol{Q}\boldsymbol{g}'}^{\boldsymbol{\xi}\dagger} F_{L\boldsymbol{Q}\boldsymbol{g}}^{\boldsymbol{\xi}} \\
&+ \sum_{\substack{LL'\boldsymbol{Q} \\ \boldsymbol{\xi gg}'}} T_{LL'}^{\boldsymbol{\xi}}(\boldsymbol{g},\boldsymbol{g}') F_{L\boldsymbol{Q}\boldsymbol{g}'}^{\boldsymbol{\xi}\dagger} F_{L\boldsymbol{Q}\boldsymbol{g}}^{\boldsymbol{\xi}} + h.c.
\end{aligned}
\tag{4.12}
$$

Here, $T_{LL'}^{\boldsymbol{\xi}}(\boldsymbol{g},\boldsymbol{g}') = T_{LL'}^{\boldsymbol{\xi}}(\boldsymbol{g}' - \boldsymbol{g})$ is used as an abbreviation.

In order diagonalize this Hamiltonian we introduce a similar basis change as in chapter 3, but with the additional mBZ lattice vector as an index $Y_{\boldsymbol{\xi}\eta\boldsymbol{Q}}^{\dagger} = \sum_{\boldsymbol{g}L} \mathcal{C}_{L\boldsymbol{g}}^{\boldsymbol{\xi}\eta*}(\boldsymbol{Q}) F_{L\boldsymbol{Q}\boldsymbol{g}}^{\boldsymbol{\xi}\dagger}$. Here, $\mathcal{C}_{L\boldsymbol{g}}^{\boldsymbol{\xi}\eta*}(\boldsymbol{Q})$ not only gives us the relative contribution between intra/interlayer excitons, but also the relative contribution between the different sub-bands that emerge due to the zone-folding. These coefficients then fulfill

$$
\begin{aligned}
\sum_{L\boldsymbol{g}} \mathcal{C}_{L\boldsymbol{g}}^{\boldsymbol{\xi}\eta_1*}(\boldsymbol{Q}) \mathcal{C}_{L\boldsymbol{g}}^{\boldsymbol{\xi}\eta_2}(\boldsymbol{Q}) &= \delta_{\eta_1\eta_2} \\
\sum_{\eta} \mathcal{C}_{L\boldsymbol{g}}^{\boldsymbol{\xi}\eta*}(\boldsymbol{Q}) \mathcal{C}_{L'\boldsymbol{g}'}^{\boldsymbol{\xi}\eta}(\boldsymbol{Q}) &= \delta_{LL'}\delta_{\boldsymbol{gg}'}.
\end{aligned}
\tag{4.13}
$$

Expanding the Hamiltonian with the mixing coefficients and summing over

the quantum index η gives us the moiré eigenvalue equation

$$
\begin{aligned}
&E_{L\boldsymbol{Q}}^{\boldsymbol{\xi}}(\boldsymbol{g})\mathcal{C}_{L\boldsymbol{g}}^{\boldsymbol{\xi}\eta}(\boldsymbol{Q}) + \sum_{\boldsymbol{g}'} V_L^{\boldsymbol{\xi}}(\boldsymbol{g},\boldsymbol{g}')\mathcal{C}_{L\boldsymbol{g}'}^{\boldsymbol{\xi}\eta}(\boldsymbol{Q}) \\
&+ \sum_{L'\boldsymbol{g}'} T_{LL'}^{\boldsymbol{\xi}}(\boldsymbol{g},\boldsymbol{g}')\mathcal{C}_{L'\boldsymbol{g}'}^{\boldsymbol{\xi}\eta}(\boldsymbol{Q}) = \mathcal{E}_{\eta\boldsymbol{Q}}^{\boldsymbol{\xi}}\mathcal{C}_{L\boldsymbol{g}}^{\boldsymbol{\xi}\eta}(\boldsymbol{Q}).
\end{aligned}
\tag{4.14}
$$

Solving this eigenvalue problem numerically will then yield us the energies for the diagonal form of the interaction-free hybrid moiré Hamiltonian

$$
H_0 = \sum_{\boldsymbol{Q}\boldsymbol{\xi}\eta} \mathcal{E}_{\eta\boldsymbol{Q}}^{\boldsymbol{\xi}} Y_{\boldsymbol{\xi}\eta\boldsymbol{Q}}^{\dagger} Y_{\boldsymbol{\xi}\eta\boldsymbol{Q}}.
\tag{4.15}
$$

4.2 Electrical and twist angle tuning of moiré excitons

We have now generalized the interaction-free Hamiltonian to include twist angles, thus allowing for one method of external tuning of the excitons landscape. We are also interested in the effects of applying on out-of-plane electric field. The addition of an external electric field is straight forward and the Hamiltonian in electron-hole basis can to leading order be approximated as

$$
H_{field} = -\sum_{\substack{\boldsymbol{k}l \\ \lambda}} e_0 z_l^{\lambda} E_z \lambda_{\boldsymbol{k}l}^{\dagger} \lambda_{\boldsymbol{k}l},
\tag{4.16}
$$

where e_0 is the elementary charge and z_l^{λ} is the real space position in z-direction of electrons (holes) in layer l. Here, E_z is the electric field strength in out-of-plane direction. By transforming this Hamiltonian into exciton basis (subsection 2.3.2), we have the following expression

$$
H_{X-l} = -\sum_{\boldsymbol{\xi}\boldsymbol{Q}L} d_L E_z X_{\boldsymbol{Q},L}^{\boldsymbol{\xi}\dagger} X_{\boldsymbol{Q},L}^{\boldsymbol{\xi}},
\tag{4.17}
$$

where $d_L = e_0 u_L$ is the dipole moment and $u_L = z_l^c - z_l^v$ the dipole length. This is intuitively understood as the potential energy of a dipole moment within an electrical field, sometimes referred to as the Stark shift of an exciton
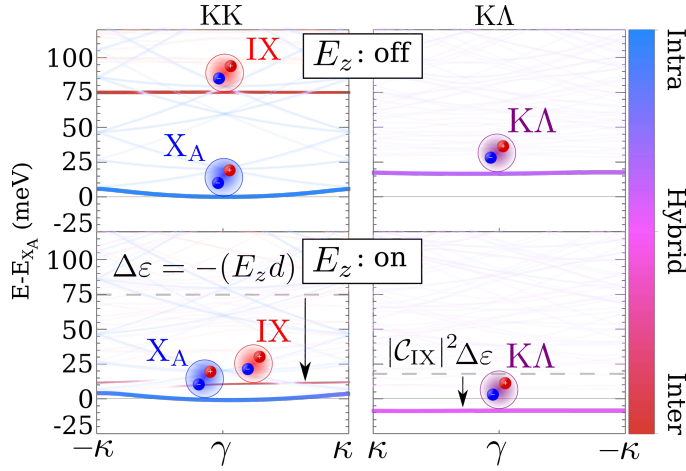
Figure 4.3: Exciton band structure for R-type stacked MoSe$_2$ homobilyer for the bright KK (left) and dark KΛ excitons (right). Multiple moiré subbands are shown in faded colors. Only the interlayer and the hybrid exciton exhibiting a dipole moment become red-shifted in presence of an electrical field (lower panel). Dashed lines indicate the original position of the corresponding excitons without an electrical field. The calculation is performed for a twist angle of $\theta = 2°$ and an electrical field of $E_z = 0.1$ V/nm.

[69, 70]. This equation can then easily be incorporated into Equation 4.7 and consequently be taken into account when solving Eq. 4.14.

In paper II. we investigated the interplay between the two presented methods for external tuning by solving Eq. 4.14. This was done for hBN encapsulated MoSe$_2$ for both R-type stacking and H-type stacking. Here, in the top row of Fig 4.3 we see the exciton bandstructure for the KK exciton and the strongly hybridized KΛ exciton in a twisted R-type structure. Both the KK interlayer exciton and the KΛ exciton are heavily affected by the periodic moiré potential and will thus exhibit a flat bandstructure. The interlayer nature of these excitons are shown via the color gradient on the right where we can clearly see the strong hybrid nature of the KΛ exciton.

By applying an electric field we will then redshift(blueshift) the excitons that exhibit an out-of-plane dipole moment. Since the hybrid KΛ exciton only partially carries an interlayer component it will have a weighted shift proportional to this component $|\mathcal{C}_{\text{IX}}|^2$. We see from the bottom row of Fig 4.3
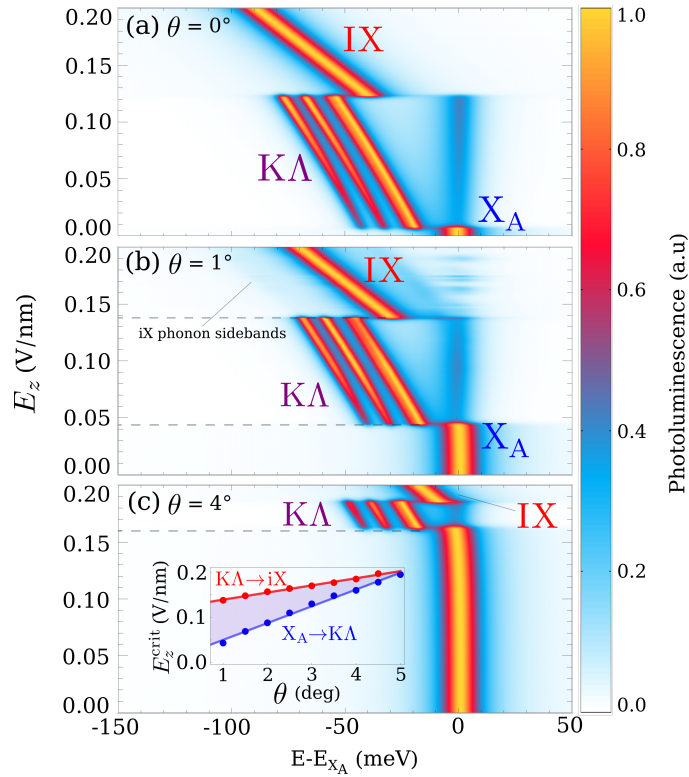
Figure 4.4: Photoluminescence spectra as a function of electrical field strength at the twist angles of (a) $\theta = 0°$, (b) $\theta = 1°$ and (c) $\theta = 4°$ at 4K. We observe three distinct energy regions, which are dominated by the A exciton X_A, the phonon sidebands of the dark $K\Lambda$ exciton and the interlayer exciton IX, respectively. The inset in (c) shows the critical electrical field strength E_z^{crit} as a function of the twist angle for the transition between different spectral regions (X_A to $K\Lambda$ and X_A to IX-dominated region). The shaded area indicates the range, where the dark $K\Lambda$ excitons dominate the PL.

that by applying an electric field we can shift the $K\Lambda$ exciton to become the lowest lying one instead of the intralayer KK, demonstrating the possibility to tune which exciton state will dominate the optical response of this material.

In Fig 4.4, the optical response for the material is calculated in the form of PL spectra. Here we sweep over the electrical field strength, consequently shifting both the $K\Lambda$ exciton and the KK interlayer exciton downwards in the bandstructure. This results in three distinct optical regions in the spectra.

By first looking at the untwisted case (cf. Fig 4.4.a) we see that the A exciton (KK intralayer) dominates at very small electric field strengths. Then rapidly the spectra changes to show phonon sidebands of the KΛ exciton. This is due to the KΛ exciton being redshifted sufficiently to gain enough occupation to dominate the optical response. By increasing the field strength even further the KK interlayer exciton IX is now dominating instead. Since the pure KK interlayer exciton is very weakly hybridized it carries a larger dipole moment and will thus have a steeper slope with respect to the electric field, guaranteeing a crossing between the KΛ exciton and IX at some point.

Furthermore, by introducing a twist angle (cf. Fig 4.4.b and Fig 4.4.c) we can tune the energetic position of the excitons that are heavily affected by the moiré potential. With the larger momentum transfer g that comes with an increased twist angle, the effects that redshifts these exciton will be suppressed, consequently shifting the IX and KΛ exciton upwards in the bandstructre. This allows us to calculate the critical fields necessary for a given twist angle when the KΛ exciton dominates the spectra. In turn we predict when the material is transformed from a direct semiconductor (KK) to an indirect semiconductor (KΛ). Moreover, by looking at smaller twist angles (cf. Fig 4.4.b) we can see additional features due to the multiple subbands that emerge in this regime. Here, the rotation of the Brillouin zone puts the energetic minimum of the interlayer exciton IX outside of the light cone, allowing for very weak phonon sidebands. The apparent oscillations that appear around the position of the A exciton is also due to the small twist angle. Here, the higher lying subbands of IX will be redshifted and hybridize with the A exciton when on top of it, consequently affecting the oscillator strength of the A exciton.

41

CHAPTER 5

CONCLUSION

In this work we have presented a fully microscopic quantum mechanical model for the exciton energy landscape and exciton optics in vertically stacked transition metal dichalcogenides. With the use of input from density functional theory we have calculated the exciton energy landscape for different homo- and heterobilayers in the presence of the moiré potential, taking into account both the hybridization component and the stacking dependent alignment shift. We reveal a strong impact from the hybridization, consequently making the momentum forbidden dark excitons the most energetically favorable in many bilayer TMDs. Furthermore, we investigate how one can tune the optical response of the exciton energy landscape in the form of twist angle engineering and applied electrical fields, in turn revealing distinct optical regions in the PL spectrum, allowing for both intra- and interlayer excitons, and even dark excitons. Moreover, we predict critical electrical fields as a function of twist angle where one can tune the material from a direct into an indirect semiconductor, which is of importance in many optoelectrical devices. Overall, the work provides microscopic insights into the twist-angle dependent exciton landscape that governs the optical response in this technologically promising class of nanomaterials.

So far we have assumed a rigid lattice model for the calculation of the exciton energy landscape. This assumption holds quite well for twist angles above

$\theta = 1°$. However, when investigating smaller twist angles the lattice will be strained to more energetically favorable stackings. Consequently, distinct regions within the moiré supercell will emerge, each region corresponding to a high symmetry stacking [71–74]. This atomic reconstruction could have a significant impact on the optical response of the material, especially in twist angles close to $\theta = 0°$. This opens up another aspect of twist tuning bilayer TMDs, were the dimensionality of the trapped excitons could potentially be tuned [75].

Furthermore, in this work we have mainly focused on the tunability of the interaction-free Hamiltonian. The introduction of a twist angle should also have a significant impact on the dynamics of excitons. Investigating how the twist angle dependent hybridization impacts the exciton-phonon scattering rate could potentially lead to interesting insights about the relaxation dynamics of these material [76]. Similarly, the moiré potential should also have a significant impact on the transport properties of excitons, which to a large degree is governed by density dependent exciton-exciton interactions [77, 78].

We have in this work investigated how one can tune the exciton energy landscape via twist angle engineering and applied electrical fields. Another way to externally tune the exciton bandstructure is by applying strain to the TMD sheet [79, 80], allowing for the Λ valley to be shifted in opposite direction with respect to the K valley. This would allow for another experimentally accessible knob when tuning the exciton energy landscape in bilayer TMDs. Especially intriguing is the interplay between atomic reconstruction and strain, where the reconstructed lattice gives rise to localized strain in the supercell and could potentially lead to a rich variation of the exciton energy landscape within the supercell itself [81].

Finally, experimental studies have reported the observation of correlated insulating states at fractional fillings when the twist angle is sufficiently small to create flat bands [82]. A microscopic study of these so-called Wigner crystals [83], taking into account the moiré excitons in twisted bilayers could potentially reveal interesting insights into the intriguing topic of correlated states in moiré structures.

BIBLIOGRAPHY

[1] Kostya S Novoselov, Andre K Geim, Sergei V Morozov, De-eng Jiang, Yanshui Zhang, Sergey V Dubonos, Irina V Grigorieva, and Alexandr A Firsov. Electric field effect in atomically thin carbon films. *science*, 306(5696):666–669, 2004.

[2] KS Novoselov. Nobel lecture: Graphene: Materials in the flatland. *Reviews of Modern Physics*, 83(3):837, 2011.

[3] AH Castro Neto, Francisco Guinea, Nuno MR Peres, Kostya S Novoselov, and Andre K Geim. The electronic properties of graphene. *Reviews of modern physics*, 81(1):109, 2009.

[4] Pablo Ares and Kostya S Novoselov. Recent advances in graphene and other 2d materials. *Nano Materials Science*, 2021.

[5] Kin Fai Mak, Changgu Lee, James Hone, Jie Shan, and Tony F. Heinz. Atomically thin MoS_2: A new direct-gap semiconductor. *Physical Review Letters*, 105:136805, 2010.

[6] Thomas Mueller and Ermin Malic. Exciton physics and device application of two-dimensional transition metal dichalcogenide semiconductors. *npj 2D Materials and Applications*, 2(1):1–12, 2018.

[7] Oriol Lopez-Sanchez, Dominik Lembke, Metin Kayci, Aleksandra Radenovic, and Andras Kis. Ultrasensitive photodetectors based on monolayer mos2. *Nature nanotechnology*, 8(7):497–501, 2013.

[8] Gang Wang, Alexey Chernikov, Mikhail M Glazov, Tony F Heinz, Xavier Marie, Thierry Amand, and Bernhard Urbaszek. Colloquium: Excitons in atomically thin transition metal dichalcogenides. *Reviews of Modern Physics*, 90(2):021001, 2018.

[9] Dmitry K Efimkin and Allan H MacDonald. Many-body theory of trion absorption features in two-dimensional semiconductors. *Physical Review B*, 95(3):035417, 2017.

[10] Raül Perea-Causin, Samuel Brem, and Ermin Malic. Trion-phonon interaction in atomically thin semiconductors. *arXiv preprint arXiv:2207.02037*, 2022.

[11] Andre K Geim and Irina V Grigorieva. Van der Waals heterostructures. *Nature*, 499(7459):419–425, 2013.

[12] Pasqual Rivera, John R Schaibley, Aaron M Jones, Jason S Ross, Sanfeng Wu, Grant Aivazian, Philip Klement, Kyle Seyler, Genevieve Clark, Nirmal J Ghimire, et al. Observation of long-lived interlayer excitons in monolayer $MoSe_2$-WSe_2 heterostructures. *Nature Communications*, 6(1):1–6, 2015.

[13] Wugang Liao, Yanting Huang, Huide Wang, and Han Zhang. Van der waals heterostructures for optoelectronics: Progress and prospects. *Applied Materials Today*, 16:435–455, 2019.

[14] Jens Kunstmann, Fabian Mooshammer, Philipp Nagler, Andrey Chaves, Frederick Stein, Nicola Paradiso, Gerd Plechinger, Christoph Strunk, Christian Schüller, Gotthard Seifert, et al. Momentum-space indirect interlayer excitons in transition-metal dichalcogenide van der waals heterostructures. *Nature Physics*, 14(8):801–805, 2018.

[15] Chenhao Jin, Eric Yue Ma, Ouri Karni, Emma C Regan, Feng Wang, and Tony F Heinz. Ultrafast dynamics in van der waals heterostructures. *Nature nanotechnology*, 13(11):994–1003, 2018.

[16] Roland Gillen and Janina Maultzsch. Interlayer excitons in mose 2/wse 2 heterostructures from first principles. *Physical Review B*, 97(16):165306, 2018.

[17] Philipp Merkl, Fabian Mooshammer, Philipp Steinleitner, Anna Girnghuber, K-Q Lin, Philipp Nagler, Johannes Holler, Christian Schüller, John M Lupton, Tobias Korn, et al. Ultrafast transition between exciton phases in van der waals heterostructures. *Nature materials*, 18(7):691–696, 2019.

[18] Pasqual Rivera, Hongyi Yu, Kyle L Seyler, Nathan P Wilson, Wang Yao, and Xiaodong Xu. Interlayer valley excitons in heterobilayers of transition metal dichalcogenides. *Nature nanotechnology*, 13(11):1004–1015, 2018.

[19] Zefang Wang, Yi-Hsin Chiu, Kevin Honz, Kin Fai Mak, and Jie Shan. Electrical tuning of interlayer exciton gases in wse2 bilayers. *Nano letters*, 18(1):137–143, 2018.

[20] Namphung Peimyoo, Thorsten Deilmann, Freddie Withers, Janire Escolar, Darren Nutting, Takashi Taniguchi, Kenji Watanabe, Alireza Taghizadeh, Monica Felicia Craciun, Kristian Sommer Thygesen, et al. Electrical tuning of optically active interlayer excitons in bilayer mos2. *Nature Nanotechnology*, 16(8):888–893, 2021.

[21] Yuan Cao, Valla Fatemi, Shiang Fang, Kenji Watanabe, Takashi Taniguchi, Efthimios Kaxiras, and Pablo Jarillo-Herrero. Unconventional superconductivity in magic-angle graphene superlattices. *Nature*, 556(7699):43–50, 2018.

[22] Kyle L Seyler, Pasqual Rivera, Hongyi Yu, Nathan P Wilson, Essance L Ray, David G Mandrus, Jiaqiang Yan, Wang Yao, and Xiaodong Xu. Signatures of moiré-trapped valley excitons in mose2/wse2 heterobilayers. *Nature*, 567(7746):66–70, 2019.

[23] Kha Tran, Galan Moody, Fengcheng Wu, Xiaobo Lu, Junho Choi, Kyounghwan Kim, Amritesh Rai, Daniel A Sanchez, Jiamin Quan, Akshay Singh, et al. Evidence for moiré excitons in van der waals heterostructures. *Nature*, 567(7746):71–75, 2019.

49

[24] Hongyi Yu, Gui-Bin Liu, Jianju Tang, Xiaodong Xu, and Wang Yao. Moiré excitons: From programmable quantum emitter arrays to spin-orbit–coupled artificial lattices. *Science advances*, 3(11):e1701696, 2017.

[25] Junho Choi, Matthias Florian, Alexander Steinhoff, Daniel Erben, Kha Tran, Dong Seob Kim, Liuyang Sun, Jiamin Quan, Robert Claassen, Somak Majumder, et al. Twist angle-dependent interlayer exciton lifetimes in van der waals heterostructures. *Physical Review Letters*, 126(4):047401, 2021.

[26] Philipp Merkl, Fabian Mooshammer, Samuel Brem, Anna Girnghuber, Kai-Qiang Lin, Leonard Weigl, Marlene Liebich, Chaw-Keong Yong, Roland Gillen, Janina Maultzsch, et al. Twist-tailoring coulomb correlations in van der waals homobilayers. *Nature communications*, 11(1):1–7, 2020.

[27] Di Huang, Junho Choi, Chih-Kang Shih, and Xiaoqin Li. Excitons in semiconductor moiré superlattices. *Nature Nanotechnology*, 17(3):227–238, 2022.

[28] Samuel Brem, Christopher Linderälv, Paul Erhart, and Ermin Malic. Tunable phases of moiré excitons in van der waals heterostructures. *Nano Letters*, 20(12):8534–8540, 2020. PMID: 32970445.

[29] Samuel Brem, Kai-Qiang Lin, Roland Gillen, Jonas M. Bauer, Janina Maultzsch, John M. Lupton, and Ermin Malic. Hybridized intervalley moiré excitons and flat bands in twisted wse2 bilayers. *Nanoscale*, 12:11088–11094, 2020.

[30] Wolfgang Nolting and William D. Brewer. *Fundamentals of Many-body Physics*. Springer Berlin, Heidelberg, 2009.

[31] J. M. Leinaas and J. Myrheim. On the theory of identical particles. *Nuovo Cim. B*, 37:1–23, 1977.

[32] James Nakamura, Shuang Liang, Geoffrey C Gardner, and Michael J Manfra. Direct observation of anyonic braiding statistics. *Nature Physics*, 16(9):931–936, 2020.

[33] M Lindberg and Stephan W Koch. Effective bloch equations for semiconductors. *Physical Review B*, 38(5):3342, 1988.

[34] Phaedon Avouris, Tony F. Heinz, and Tony Low, editors. *2D Materials: Properties and Devices*. Cambridge University Press, 2017.

[35] Andor Kormányos, Guido Burkard, Martin Gmitra, Jaroslav Fabian, Viktor Zólyomi, Neil D Drummond, and Vladimir Fal'ko. k· p theory for two-dimensional transition metal dichalcogenide semiconductors. *2D Materials*, 2(2):022001, 2015.

[36] Xiaodong Li, Jeffrey T Mullen, Zhenghe Jin, Kostyantyn M Borysenko, M Buongiorno Nardelli, and Ki Wook Kim. Intrinsic electrical transport properties of monolayer silicene and mos 2 from first principles. *Physical Review B*, 87(11):115418, 2013.

[37] Mackillo Kira and Stephan W. Koch. *Semiconductor Quantum Optics*. Cambridge University Press, 2011.

[38] Natalia S Rytova. Screened potential of a point charge in a thin film. *Moscow University Physics Bulletin*, 3(30), 1967.

[39] LV Keldysh. Coulomb interaction in thin semiconductor and semimetal films. *Soviet Journal of Experimental and Theoretical Physics Letters*, 29:658, 1979.

[40] Samuel Brem, Jonas Zipfel, Malte Selig, Archana Raja, Lutz Waldecker, Jonas D Ziegler, Takashi Taniguchi, Kenji Watanabe, Alexey Chernikov, and Ermin Malic. Intrinsic lifetime of higher excitonic states in tungsten diselenide monolayers. *Nanoscale*, 11(25):12381–12387, 2019.

[41] Zhenghe Jin, Xiaodong Li, Jeffrey T Mullen, and Ki Wook Kim. Intrinsic transport properties of electrons and holes in monolayer transition-metal dichalcogenides. *Physical Review B*, 90(4):045422, 2014.

[42] Jamie M Fitzgerald, Joshua JP Thompson, and Ermin Malic. Twist angle tuning of moiré exciton polaritons in van der waals heterostructures. *Nano Letters*, 2022.

[43] Beatriz Ferreira, Roberto Rosati, and Ermin Malic. Microscopic modeling of exciton-polariton diffusion coefficients in atomically thin semiconductors. *Physical Review Materials*, 6(3):034008, 2022.

[44] Raul Perea-Causin, Samuel Brem, Roberto Rosati, Roland Jago, Marvin Kulig, Jonas D Ziegler, Jonas Zipfel, Alexey Chernikov, and Ermin Malic. Exciton propagation and halo formation in two-dimensional materials. *Nano letters*, 19(10):7317–7323, 2019.

[45] Ermin Malic, Malte Selig, Maja Feierabend, Samuel Brem, Dominik Christiansen, Florian Wendler, Andreas Knorr, and Gunnar Berghäuser. Dark excitons in transition metal dichalcogenides. *Physical Review Materials*, 2(1):014002, 2018.

[46] Gunnar Berghäuser, Philipp Steinleitner, Philipp Merkl, Rupert Huber, Andreas Knorr, and Ermin Malic. Mapping of the dark exciton landscape in transition metal dichalcogenides. *Physical Review B*, 98(2):020301, 2018.

[47] Robert Wallauer, Raul Perea-Causin, Lasse Münster, Sarah Zajusch, Samuel Brem, Jens Güdde, Katsumi Tanimura, Kai-Qiang Lin, Rubert Huber, Ermin Malic, et al. Momentum-resolved observation of exciton formation dynamics in monolayer ws2. *Nano Letters*, 21(13):5867–5873, 2021.

[48] Florian Katsch, Malte Selig, Alexander Carmele, and Andreas Knorr. Theory of exciton–exciton interactions in monolayer transition metal dichalcogenides. *physica status solidi (b)*, 255(12):1800185, 2018.

[49] M Kira and SW Koch. Many-body correlations and excitonic effects in semiconductor spectroscopy. *Progress in Quantum Electronics*, 30(5):155–296, 2006.

[50] Jonas Kiemle, Florian Sigger, Michael Lorke, Bastian Miller, Kenji Watanabe, Takashi Taniguchi, Alexander Holleitner, and Ursula Wurstbauer. Control of the orbital character of indirect excitons in mos 2/ws 2 heterobilayers. *Physical Review B*, 101(12):121404, 2020.

[51] Ying Jiang, Shula Chen, Weihao Zheng, Biyuan Zheng, and Anlian Pan. Interlayer exciton formation, relaxation, and transport in tmd van der waals heterostructures. *Light: Science & Applications*, 10(1):1–29, 2021.

[52] Simon Ovesen, Samuel Brem, Christopher Linderälv, Mikael Kuisma, Tobias Korn, Paul Erhart, Malte Selig, and Ermin Malic. Interlayer

exciton dynamics in van der waals heterostructures. *Communications Physics*, 2(1):1–8, 2019.

[53] Akash Laturia, Maarten L Van de Put, and William G Vandenberghe. Dielectric properties of hexagonal boron nitride and transition metal dichalcogenides: from monolayer to bulk. *npj 2D Materials and Applications*, 2(1):1–7, 2018.

[54] F. Ferreira, S. J. Magorrian, V. V. Enaldiev, D. A. Ruiz-Tijerina, and V. I. Fal'ko. Band energy landscapes in twisted homobilayers of transition metal dichalcogenides. *Applied Physics Letters*, 118(24):241602, 2021.

[55] Qingjun Tong, Mingxing Chen, Feiping Xiao, Hongyi Yu, and Wang Yao. Interferences of electrostatic moiré potentials and bichromatic superlattices of electrons and excitons in transition metal dichalcogenides. *2D Materials*, 8(2):025007, 2020.

[56] Christopher Linderälv, Joakim Hagel, Samuel Brem, Ermin Malic, and Paul Erhart. The moiré potential in twisted transition metal dichalcogenide bilayers. *arXiv preprint arXiv:2205.15616*, 2022.

[57] Qingjun Tong, Mingxing Chen, Feiping Xiao, Hongyi Yu, and Wang Yao. Interferences of electrostatic moiré potentials and bichromatic superlattices of electrons and excitons in transition metal dichalcogenides. *2D Materials*, 8(2):025007, dec 2020.

[58] Evgeny M Alexeev, David A Ruiz-Tijerina, Mark Danovich, Matthew J Hamer, Daniel J Terry, Pramoda K Nayak, Seongjoon Ahn, Sangyeon Pak, Juwon Lee, Jung Inn Sohn, et al. Resonantly hybridized excitons in moiré superlattices in van der waals heterostructures. *Nature*, 567(7746):81–86, 2019.

[59] Iann C Gerber, Emmanuel Courtade, Shivangi Shree, Cedric Robert, Takashi Taniguchi, Kenji Watanabe, Andrea Balocchi, Pierre Renucci, Delphine Lagarde, Xavier Marie, et al. Interlayer excitons in bilayer mos 2 with strong oscillator strength up to room temperature. *Physical Review B*, 99(3):035443, 2019.

[60] David A. Ruiz-Tijerina and Vladimir I. Fal'ko. Interlayer hybridization and moiré superlattice minibands for electrons and excitons in hetero-bilayers of transition-metal dichalcogenides. *Phys. Rev. B*, 99:125424, Mar 2019.

[61] Yong Wang, Zhan Wang, Wang Yao, Gui-Bin Liu, and Hongyi Yu. Inter-layer coupling in commensurate and incommensurate bilayer structures of transition-metal dichalcogenides. *Physical Review B*, 95(11):115429, 2017.

[62] E Cappelluti, Rafael Roldán, JA Silva-Guillén, Pablo Ordejón, and F Guinea. Tight-binding model and direct-gap/indirect-gap transition in single-layer and multilayer mos 2. *Physical Review B*, 88(7):075409, 2013.

[63] David A Ruiz-Tijerina and Vladimir I Fal'ko. Interlayer hybridiza-tion and moiré superlattice minibands for electrons and excitons in heterobilayers of transition-metal dichalcogenides. *Physical Review B*, 99(12):125424, 2019.

[64] Samuel Brem, August Ekman, Dominik Christiansen, Florian Katsch, Malte Selig, Cedric Robert, Xavier Marie, Bernhard Urbaszek, Andreas Knorr, and Ermin Malic. Phonon-assisted photoluminescence from in-direct excitons in monolayers of transition-metal dichalcogenides. *Nano Letters*, 20(4):2849–2856, 2020. PMID: 32084315.

[65] Daniel Erkensten, Samuel Brem, and Ermin Malic. Exciton-exciton interaction in transition metal dichalcogenide monolayers and van der waals heterostructures. *Physical Review B*, 103(4):045426, 2021.

[66] Daniel Erkensten, Samuel Brem, Koloman Wagner, Roland Gillen, Raül Perea-Causín, Jonas D Ziegler, Takashi Taniguchi, Kenji Watanabe, Janina Maultzsch, Alexey Chernikov, et al. Dark exciton-exciton an-nihilation in monolayer wse 2. *Physical Review B*, 104(24):L241406, 2021.

[67] Malte Selig, Gunnar Berghäuser, Archana Raja, Philipp Nagler, Chris-tian Schüller, Tony F Heinz, Tobias Korn, Alexey Chernikov, Ermin Malic, and Andreas Knorr. Excitonic linewidth and coherence lifetime

in monolayer transition metal dichalcogenides. *Nature communications*, 7(1):1–6, 2016.

[68] Hong EnáLim et al. Restoring the intrinsic optical properties of cvd-grown mos 2 monolayers and their heterostructures. *Nanoscale*, 11(27):12798–12803, 2019.

[69] Nadine Leisgang, Shivangi Shree, Ioannis Paradisanos, Lukas Sponfeldner, Cedric Robert, Delphine Lagarde, Andrea Balocchi, Kenji Watanabe, Takashi Taniguchi, Xavier Marie, et al. Giant stark splitting of an exciton in bilayer mos2. *Nature Nanotechnology*, 15(11):901–907, 2020.

[70] Yuanda Liu, Kévin Dini, Qinghai Tan, Timothy Liew, Kostya S Novoselov, and Weibo Gao. Electrically controllable router of interlayer excitons. *Science advances*, 6(41):eaba1830, 2020.

[71] V. V. Enaldiev, V. Zólyomi, C. Yelgel, S. J. Magorrian, and V. I. Fal'ko. Stacking domains and dislocation networks in marginally twisted bilayers of transition metal dichalcogenides. *Phys. Rev. Lett.*, 124:206101, May 2020.

[72] V V Enaldiev, F Ferreira, S J Magorrian, and Vladimir I Fal'Ko. Piezoelectric networks and ferroelectric domains in twistronic superlattices in ws2/mos2 and wse2/mose2 bilayers. *2D Materials*, 8(2):025030, 2021.

[73] Hyobin Yoo, Rebecca Engelke, Stephen Carr, Shiang Fang, Kuan Zhang, Paul Cazeaux, Suk Hyun Sung, Robert Hovden, Adam W Tsen, Takashi Taniguchi, et al. Atomic and electronic reconstruction at the van der waals interface in twisted bilayer graphene. *Nature materials*, 18(5):448–453, 2019.

[74] Stephen Carr, Daniel Massatt, Steven B. Torrisi, Paul Cazeaux, Mitchell Luskin, and Efthimios Kaxiras. Relaxation and domain formation in incommensurate two-dimensional heterostructures. *Phys. Rev. B*, 98:224102, Dec 2018.

[75] V V Enaldiev, F Ferreira, J G McHugh, and Vladimir I Fal'Ko. Self-organised quantum dots in marginally twisted mose$_2$/wse$_2$ and mos$_2$/ws$_2$ bilayers. *arXiv preprint arXiv:2204.06823*, 2022.

[76] Giuseppe Meneghini, Samuel Brem, and Ermin Malic. Ultrafast phonon-driven charge transfer in van der waals heterostructures. *Natural Sciences*, page e20220014, 2022.

[77] Daniel Erkensten, Raül Perea-Causin, Samuel Brem, and Ermin Malic. Microscopic origin of anomalous interlayer exciton transport in van der Waals heterostructures. *arXiv preprint arXiv:2207.03942*, 2022.

[78] Long Yuan, Biyuan Zheng, Jens Kunstmann, Thomas Brumme, Agnieszka Beata Kuc, Chao Ma, Shibin Deng, Daria Blach, Anlian Pan, and Libai Huang. Twist-angle-dependent interlayer exciton diffusion in ws2–wse2 heterobilayers. *Nature materials*, 19(6):617–623, 2020.

[79] Maja Feierabend, Alexandre Morlet, Gunnar Berghäuser, and Ermin Malic. Impact of strain on the optical fingerprint of monolayer transition-metal dichalcogenides. *Physical Review B*, 96(4):045425, 2017.

[80] Roberto Rosati, Robert Schmidt, Samuel Brem, Raül Perea-Causín, Iris Niehues, Johannes Kern, Johann A Preuß, Robert Schneider, Steffen Michaelis de Vasconcellos, Rudolf Bratschitsch, et al. Dark exciton anti-funneling in atomically thin semiconductors. *Nature Communications*, 12(1):1–7, 2021.

[81] Nathanael P Kazmierczak, Madeline Van Winkle, Colin Ophus, Karen C Bustillo, Stephen Carr, Hamish G Brown, Jim Ciston, Takashi Taniguchi, Kenji Watanabe, and D Kwabena Bediako. Strain fields in twisted bilayer graphene. *Nature materials*, 20(7):956–963, 2021.

[82] Yang Xu, Song Liu, Daniel A Rhodes, Kenji Watanabe, Takashi Taniguchi, James Hone, Veit Elser, Kin Fai Mak, and Jie Shan. Correlated insulating states at fractional fillings of moiré superlattices. *Nature*, 587(7833):214–218, 2020.

[83] Samuel Brem and Ermin Malic. Terahertz fingerprint of monolayer wigner crystals. *Nano letters*, 22(3):1311–1315, 2022.